

# Geochemistry, Geophysics, Geosystems

## RESEARCH ARTICLE

10.1029/2019GC008219

### Key Points:

- Proposed stress states for the southern end of the Malawi Rift are tested by assessing fault reactivation potential
- Variably oriented faults reactivate by all striking slightly obliquely to an ENE-WSW to E-W trending minimum principal compressive stress
- Faults may locally accommodate pure normal dip slip due to the presence of a deep seated crustal weakness

### Supporting Information:

- Supporting Information S1

### Correspondence to:

J. N. Williams,  
williamsj132@cardiff.ac.uk

### Citation:

Williams, J. N., Fagereng, Å., Wedmore, L. N. J., Biggs, J., Mphepo, F., Dulanya, Z., et al. (2019). How do variably striking faults reactivate during rifting? Insights from southern Malawi. *Geochemistry, Geophysics, Geosystems*, 20, 3588–3607. <https://doi.org/10.1029/2019GC008219>

Received 23 JAN 2019

Accepted 26 MAY 2019

Accepted article online 3 JUL 2019

Published online 25 JUL 2019

## How Do Variably Striking Faults Reactivate During Rifting? Insights From Southern Malawi

Jack N. Williams<sup>1</sup> , Åke Fagereng<sup>1</sup> , Luke N. J. Wedmore<sup>2</sup> , Juliet Biggs<sup>2</sup> , Felix Mphepo<sup>3</sup>, Zuze Dulanya<sup>4</sup>, Hassan Mdala<sup>3</sup>, and Thomas Blenkinsop<sup>1</sup> 

<sup>1</sup>School of Earth and Ocean Sciences, Cardiff University, Cardiff, UK, <sup>2</sup>School of Earth Sciences, University of Bristol, Bristol, UK, <sup>3</sup>Geological Survey Department, Mzuzu Regional Office, Mzuzu, Malawi, <sup>4</sup>Geography and Earth Sciences Department, University of Malawi, Zomba, Malawi

**Abstract** Crustal extension is commonly thought to be accommodated by faults that strike orthogonal and obliquely to the regional trend of the minimum compressive stress ( $\sigma_3$ ). Activation of oblique faults can, however, be conceptually problematic as under Andersonian faulting, it requires preexisting crustal weaknesses, high fluid pressures, and/or stress rotations. Furthermore, measurements of incremental fault displacements, which are typically used to identify oblique faulting, do not necessarily reflect regional stresses. Here, we assess oblique faulting by calculating the stress ratio ( $\sigma_3/\sigma_1$ , where  $\sigma_1$  is the maximum compressive stress), slip tendency, and effective coefficient of friction ( $\mu_s'$ ) required to reactivate variably striking normal faults under different trends of  $\sigma_3$ . We apply this analysis to NW and NNE striking active faults at the southern end of the Malawi Rift, where NE-SW, ENE-WSW, E-W, and SE-NW  $\sigma_3$  trends have previously been proposed. A uniform  $\sigma_3$  trend is inferred for this region as recent joint sets do not rotate along the rift. With a NE-SW trending  $\sigma_3$ , NW-striking faults are well oriented, however, NNE-striking faults require  $\mu_s' < 0.6$  to reactivate. This is inconsistent with a lack of frictionally weak phyllosilicates detected in the fault zone rocks. With an ENE-WSW to E-W trending  $\sigma_3$ , all faults can reactivate at  $\mu_s' > 0.55$ . These  $\sigma_3$  trends are also comparable to a focal mechanism stress inversion, regional joint orientations, and previously reported geodetically derived extension directions. We therefore conclude that unlike typical models of oblique rifting, the southern Malawi Rift consists of faults that all strike slightly oblique to  $\sigma_3$ .

**Plain Language Summary** Stretching of the upper brittle part of the Earth's crust should be accommodated by fractures (faults) oriented at  $90^\circ$  to the stretching direction. However, this idealized scenario is rarely observed because of crustal heterogeneities, or because the stretching direction rotates over geological time. Thus, faults are often nonorthogonal (i.e., oblique) to the stretching direction. Here, we use a mechanical analysis to test the obliquity of faults in southern Malawi at the southern juvenile end of the East African Rift system where the crust is actively extending at  $\sim 2$  mm/year. This section is of interest as fault orientation varies along the rift, and a range of stretching directions have been proposed previously. Our mechanical analysis indicates that extension is most likely accommodated in southern Malawi by faults that are all slightly oblique to an ENE-WSW to E-W stretching direction. This is in contrast to previous models of oblique extension, which suggest that stretching is accommodated by some faults at  $90^\circ$  to the stretching direction, while others are at a very low ( $<40^\circ$ ) angle to stretching.

## 1. Introduction

Faults in continental rifts often exhibit a wide range of orientations, which can be rationalized in terms of the angle ( $\alpha$ ) between fault strike and the trend of the minimum principal compressive stress ( $\sigma_3$ ). In this context, one set of faults commonly strikes orthogonal to  $\sigma_3$  (i.e.,  $\alpha \sim 90^\circ$ ), and another set strikes highly obliquely to  $\sigma_3$  ( $\alpha < 45^\circ$ ). This rifting style has been proposed for the East African Rift System (EARS; Corti, 2012; Delvaux, 2001; Smith & Mosley, 1993), Rio Grande Rift (Aldrich, 1986), Rhine Graben (Chorowicz & Deffontaines, 1993; Lopes Cardozo & Behrmann, 2006), and the Taupō Rift (Villamor et al., 2017) and has been replicated in analog and numerical models (Acocella et al., 1999; Brune, 2014; McClay & White, 1995; Withjack & Jamison, 1986).

There is, however, a fault mechanics problem with the presence of two different sets of fault strikes in continental rifts, as under an Andersonian normal fault stress state and typical rock frictional coefficients (0.6–0.8; Byerlee, 1978),  $\alpha$  should be consistently  $\sim 90^\circ$ . Oblique fault reactivation therefore requires either

preexisting cohesionless (Etheridge, 1986; Morley et al., 2004) or frictionally weak planes (Massironi et al., 2011) and/or stress state rotations in time (Bellahsen et al., 2006; Henstra et al., 2015) or space (Morley, 2010).

Alternatively, observations of oblique faulting may simply reflect the challenges of determining regional stress directions. Typically, these are inferred from measurements of incremental fault strain (i.e., fault slickensides and earthquake focal mechanisms), which is justified by the prediction that fault slip is parallel to the direction of maximum resolved shear stress on a plane (Bott, 1959; Wallace, 1951). However, this “Wallace-Bott criterion” can break down (Pollard et al., 1993; Twiss & Unruh, 1998), including cases where rift faults that strike oblique to the regional  $\sigma_3$  trend accommodate pure normal dip slip (Corti et al., 2013; Morley, 2010; Petit et al., 1996; Philippon et al., 2015). Deriving stress states in rifts from fault slickensides is further complicated because dip slip faults can host oblique slip and even strike slip components due to convergent patterns of coseismic slip (Hampel et al., 2013; Philippon et al., 2015; Roberts, 1996). Therefore, the use of these measurements to infer that a fault is oblique is not necessarily justified.

In this study, we analyze oblique faulting by assuming a priori different stress states, and then interpreting their applicability in terms of fault reactivation potential. We use the southern end of the Malawi Rift (Figure 1) as a case example, as geological maps (Bloomfield & Garson, 1965; Habgood et al., 1973; Walshaw, 1965), fault scarps (Hodge et al., 2018, 2019; Jackson & Blenkinsop, 1997; Wedmore et al., 2019), and earthquake focal mechanisms (Delvaux & Barth, 2010) demonstrate that active faults switch from NW-SE striking in the Makanjira Graben to NNE-SSW in the Zomba Graben and then back to NW-SE in the Lower Shire Graben as the rift follows an arcuate bend in the high grade metamorphic foliation (Figure 2a). Furthermore, there is an inconsistency in the regional  $\sigma_3$  trend when inferred from fault slickensides (Chorowicz & Sorlien, 1992; Delvaux et al., 2012), fault geometry (Mortimer et al., 2007), earthquake focal mechanisms (Delvaux & Barth, 2010), and geodesy (Stamps et al., 2018). Here, four possible stress states are considered:

1. Stress State 1:  $\sigma_3$  trends SW (06/242, minimum horizontal stress ( $S_{hmin}$ ) = 00/062, Figure 2d), as proposed by an earthquake focal mechanism stress inversion for the Malawi Rift (Delvaux & Barth, 2010). In this way,  $\alpha$  is  $\sim 90^\circ$  and  $\sim 40^\circ$  for NW-striking and NNE-striking faults respectively.
2. Stress State 2: an ENE-WSW trending  $\sigma_3$  (10/072, Figure 2e), consistent with individual GPS stations in the Malawi Rift (Figure 1; Stamps et al., 2018) and an updated Malawi rift-wide focal mechanism stress inversion (section 3.2). In this case,  $\alpha > 50^\circ$  for all faults.
3. Stress State 3: an E-W trending  $\sigma_3$  (00/082, Figure 2f), which is consistent with the extension direction inferred from EARS scale geodetic models (Stamps et al., 2018) and regional joint orientations (Figure 2c). Thus, both faults sets form slightly oblique to  $\sigma_3$  ( $\alpha > 60^\circ$ ).
4. Stress State 4: stress is spatially heterogenous in southern Malawi, with Proterozoic fabrics actively rotating  $\sigma_3$  along the rift so that  $\alpha$  is consistently  $\sim 90^\circ$  (Figure 2g; Morley, 2010).

The reactivation potential of three differently oriented faults in these stress states is then quantified by their stress ratio, slip tendency, and effective coefficient of friction. By comparing these results to the frictional properties of the faults inferred from new field observations and compositional analysis, and deformation experiments performed by Hellebrekers et al. (2019), we can determine which stress state is most applicable in southern Malawi. In doing so, new insights are gained into the applicability of using incremental fault strain measurements in stress inversions, and on the controls on fault geometry in an incipient rift.

## 2. Geological Setting of the Southern Malawi Rift

The Malawi Rift is a 900-km long section of the EARS Western Branch, and runs from the Rungwe Volcanic Province (RVP) to the Urema Graben (Figures 1 and 2; Ebinger et al., 1987). It can be divided along its axis into a series of 100- to 150-km long grabens and half grabens with alternating polarities (Ebinger, 1989; Ebinger et al., 1987; Flannery & Rosendahl, 1990; Lañ-Dávila et al., 2015). The focus of this study are the three southernmost grabens: the Lower Shire, Zomba, and Makanjira grabens (Figure 2a).

Basement rock within these grabens constitute part of the Southern Irumide Belt (Figure 1), a structurally complex Mesoproterozoic orogenic belt that underwent amphibolite-granulite facies metamorphism during the Pan African orogeny ( $\sim 800$ – $450$  Ma.; Kröner et al., 2001; Johnson et al., 2006; Fritz et al., 2013). Whether

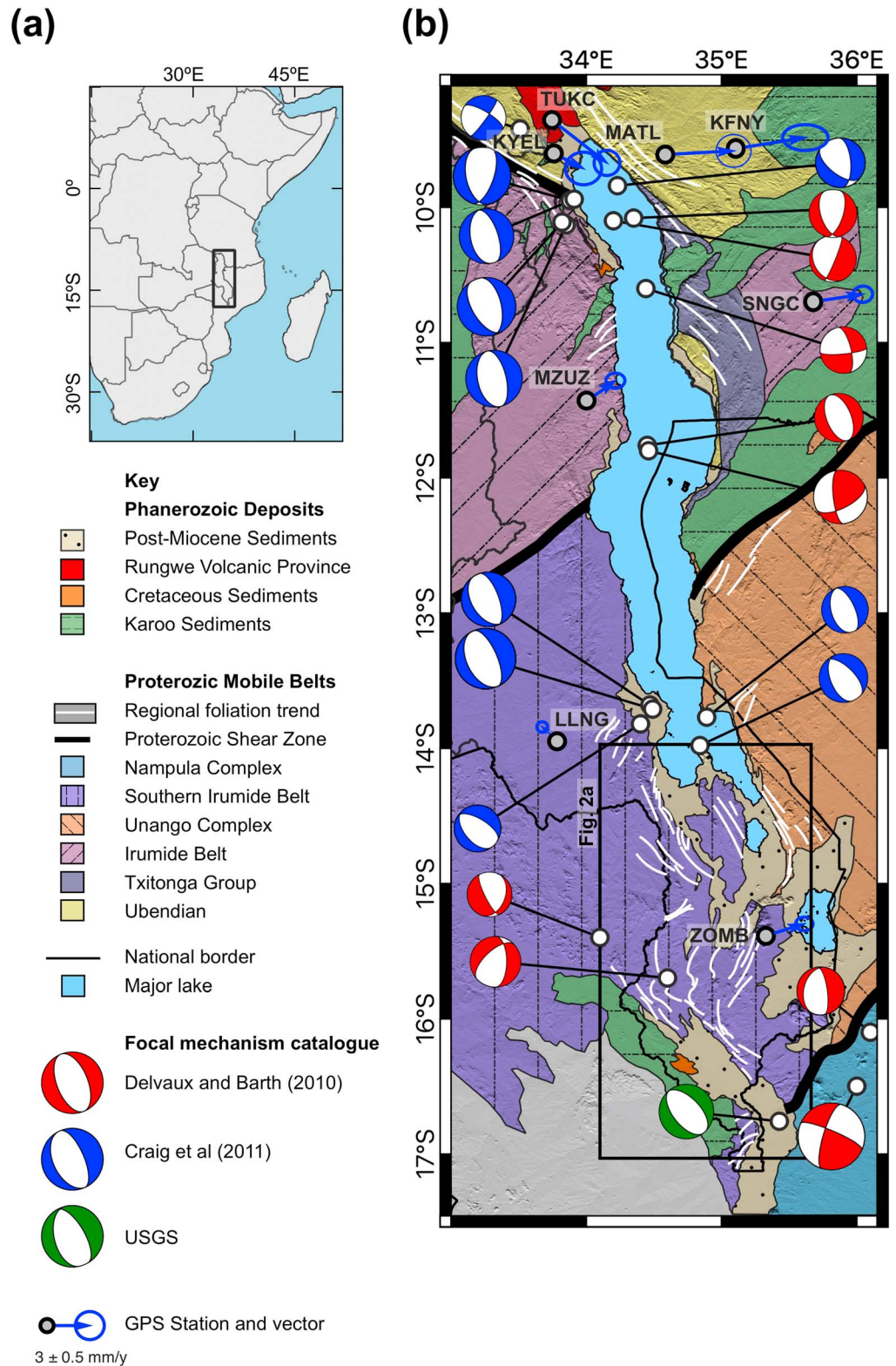


**Figure 1.** (a) Location of the Malawi Rift within East Africa. (b) Simplified geological map of the rift with Proterozoic units after Fritz et al. (2013) and underlain by Shuttle Radar Topography Mission 30-m digital elevation model (Sandwell et al., 2011). Location of focal mechanisms listed in Table 1 and vectors from GPS stations for a fixed Nubia Plate reference frame reported by Stamps et al. (2018) also given. Foliation trends collated from SRTM images, field measurements, and previous studies (Bloomfield, 1958, 1965; Bloomfield & Garson, 1965; Habgood et al., 1973; Hodge et al., 2018).

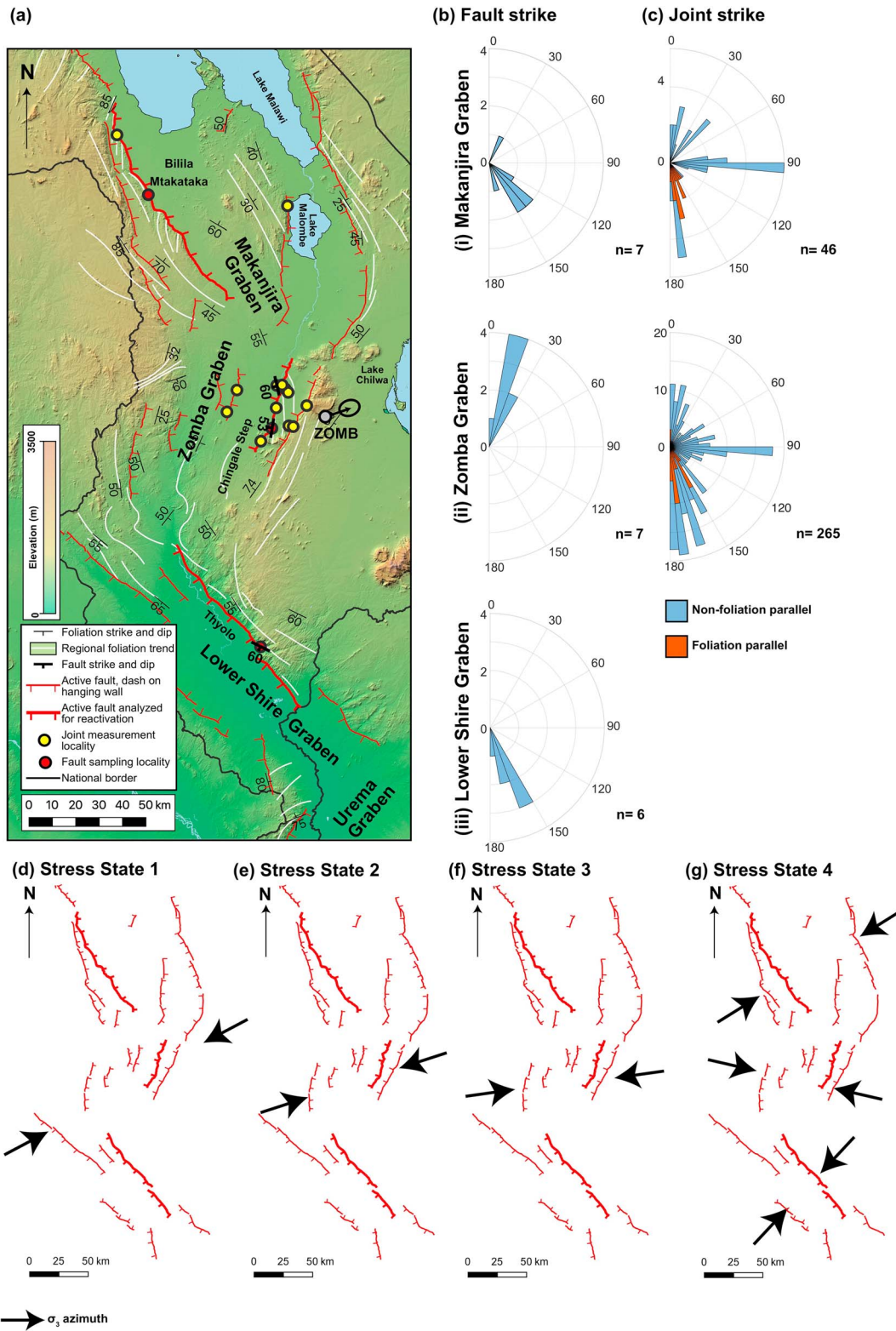


**Figure 2.** (a) Map of active faults in southern Malawi collated from TANDEM-X digital elevation model and geological maps (Bloomfield, 1958, 1965; Bloomfield & Garson, 1965; Habgood et al., 1973; Hodge et al., 2018, 2019; Walshaw, 1965; Wedmore et al., 2019). Area shown is indicated in Figure 1b. The azimuth of the ZOMB GPS station (Stamps et al., 2018), and joint and fault field localities are also shown. Rose plots for measurements of (b) fault and (c) joint strike for each of the grabens. (d–g) Schematic representation of the minimum horizontal stress ( $S_{hmin}$ ) azimuth in Stress States 1–4 with respect to faults in southern Malawi. Area shown for each map is the same as in (a). Weighted fault lines are those in which reactivation analysis was conducted.

this belt experienced earlier Irumide age deformation (~1,020–950 Ma) is unclear (Andreoli, 1984; Fritz et al., 2013; Johnson et al., 2006; Kröner et al., 2001; Manda et al., 2019) and the Lower Shire graben may strictly be part of the Neoproterozoic Zambezi Belt (Chorowicz & Sorlien, 1992; Hargrove et al., 2003; Laõ-Dávila et al., 2015). The Lower Shire Graben also underwent NW-SE Karoo extension (Castaing, 1991; Habgood, 1963), whereas this extension was comparatively minor further north in the Zomba Graben (Bloomfield, 1965). This was followed by a major period of Upper Jurassic-Lower Cretaceous magmatism throughout southern Malawi, which formed the Chilwa Alkaline Province (Bloomfield, 1965; Castaing, 1991; Dulanya, 2017; Eby et al., 1995; Habgood, 1963).

$^{40}\text{Ar}/^{39}\text{Ar}$  dating of the RVP and low temperature thermochronology indicate that the northern part of the Malawi Rift was established by the Oligocene (Mesko et al., 2014; Mortimer et al., 2016; Roberts et al., 2012); however, there is little chronostratigraphic control on the southern grabens analyzed here (Dulanya, 2017). As elsewhere in the EARS (Smith & Mosley, 1993; Versfelt & Rosendahl, 1989), these grabens follow the regional moderately dipping foliation (Figure 2a). Thus, a polymodal range (sensu Healy et al., 2015) of NW to NNE striking faults occurs in southern Malawi.

### 3. Strain and Stress Indicators Within the Malawi Rift

#### 3.1. Previous Estimates of Strain and Stress Within the Malawi Rift

At the scale of the EARS, kinematic models have been developed using a combination of earthquake slip vectors, and continuous and campaign GPS measurements (Saria et al., 2014; Stamps et al., 2008, 2018). For the Malawi Rift, these models indicate an extension azimuth of  $086^\circ \pm 5^\circ$  relative to a fixed Nubia Plate (Saria et al., 2014; Stamps et al., 2018). However, the azimuth of individual GPS stations in the rift indicate ENE-WSW extension, except in the vicinity of the RVP (Figure 1; Stamps et al., 2018).

Delvaux and Barth (2010) used an earthquake focal mechanism stress inversion to derive a near Andersonian normal fault stress state for the Malawi Rift, with a subvertical maximum compressive principal stress ( $\sigma_1$ , 83/070) and subhorizontal  $\sigma_3$  (06/242,  $S_{\text{hmin}} = 00/062$ ). This  $S_{\text{hmin}}$  orientation implies NE-SW extension, which is supported by slickenside measurements in the northern part of the Malawi Rift (Delvaux et al., 2012) but differs by  $10^\circ$  to  $20^\circ$  from the extension directions inferred from geodetic data (Stamps et al., 2018). Furthermore, this stress inversion predicts that NNE-striking faults accommodate oblique extension (Figure 2d). However, slickensides on these faults indicate nearly pure dip-slip motion and thus approximately NW-SE extension (Bloomfield & Garson, 1965; Chorowicz & Sorlien, 1992; Ring et al., 1992; Wedmore et al., 2019). The geometry of faults from seismic reflection surveys within Lake Malawi has also been used to infer NW-SE rift extension (Mortimer et al., 2007; Scott et al., 1992).

#### 3.2. An Updated Stress Inversion for the Malawi Rift

The discrepancy in rift extension direction when inferred from earthquake focal mechanisms, geodetic data, or fault slickensides may reflect the high azimuthal error and limited data set (13 focal mechanisms across the 900-km long rift) used by Delvaux and Barth (2010). We therefore performed an inversion with an expanded catalog of 21 focal mechanisms (Table 1 and Figure 1a), which incorporates (1) the four mainshocks ( $M_{\text{W}}$  5.5–5.9) of the 2009 Karonga earthquake sequence (Biggs et al., 2010; Gaherty et al., 2019; Hamiel et al., 2012), (2) the 2018  $M_{\text{W}}$  5.5 Nsanje earthquake (U.S. Department of the Interior U.S. Geological Survey, 2018), and (3) focal mechanisms from revised bodywave modeling (Craig et al., 2011), which are considered more accurate than the Global Centroid Moment Tensor solutions used in the Delvaux and Barth (2010) inversion.

As in Delvaux and Barth (2010), we use Win-Tensor (version 5.8.8, Delvaux & Sperner, 2003) to perform the inversion. Here, the data are first processed using the “Right Dihedron Method” to determine the possible range of  $\sigma_1$  and  $\sigma_3$  orientations (Angelier & Mechler, 1977). This range is then refined by using “Rotational Optimisation” (Delvaux & Sperner, 2003), which seeks to reduce the misfit angle ( $\omega$ ) between the earthquake slip vectors and the azimuth of maximum shear stress within the inversion. This inversion is first run for both nodal planes and then subsequently with just the plane that has the smallest misfit. Focal mechanisms were progressively filtered during the Right Dihedron method analysis using the Counting Deviation method (Delvaux & Sperner, 2003, see supporting information Text S1).

**Table 1**  
Compilation of Earthquake Focal Mechanisms for the Malawi Rift

Event	Date (yyyy/mm/dd)	$M_w$	Longitude	Latitude	Depth (km)	Catalog	Strike	Dip	Rake	Rejected	Misfit (deg)	Notes
a	1954/01/17	6.7	36.00	-16.50	20	DB2010	197	68	164	Y		
b	1966/05/06	5.1	34.60	-15.70	17	DB2010	001	51	-56		38.4	
c	1978/01/08	4.9	34.45	-11.76	15	DB2010	158	45	-90		1.9	
d	1989/03/09	5.5	34.47	-13.68	31	C2011	340	56	-99	Y		Same as event 4 in DB2010
e	1989/03/10	6.1	34.49	-13.71	32	C2011	336	56	-92		5.9	Same as event 5 in DB2010
f	1989/09/05	5.4	34.46	-11.80	19.8	DB2010	063	52	149	Y		
g	1994/11/16	4.5	33.51	-9.42	7	C2011	301	64	-11	Y		Focal mechanism from gCMT
h	1995/07/22	4.9	34.84	-13.98	33	C2011	158	42	-105		19.1	
i	1995/09/30	4.7	34.40	-13.82	30	C2011	321	54	-75		2.6	
j	1996/08/30	4.5	34.10	-15.40	10	DB2010	154	71	-109		2.6	
k	1998/08/24	4.7	34.89	-13.77	44	C2011	163	37	-95		3.8	Same as event 7 in DB2010
l	1999/09/01	4.7	34.20	-10.10	10	DB2010	022	81	-144	Y		
m	2000/01/04	4.8	36.10	-16.10	25	DB2010	352	66	-70		13.8	
n	2002/08/31	5.0	34.23	-9.84	20	C2011	355	53	-126		29.7	Same as event 9 in DB2010
o	2004/03/14	4.8	34.35	-10.08	29	DB2010	017	52	-117		14.0	
p	2004/08/21	4.7	34.44	-10.60	12	DB2010	084	75	-17		6.1	
q	2009/12/06	5.7	33.85	-10.13	6	C2011	168	38	-91		4.8	
r	2009/12/09	5.8	33.88	-9.95	6	C2011	167	41	-70		31.1	
s	2009/12/12	5.5	33.91	-9.94	4	C2011	169	37	-95		0.8	
t	2009/12/19	5.9	33.82	-10.11	5	C2011	149	46	-77		2.8	
u	2018/03/08	5.5	35.427	-16.760	17	USGS	316	45	-94	Y		

*Note.* Catalog codes are (1) DB2010, Delvaux and Barth (2010) and references therein, (2) C2011, Craig et al. (2011) and references therein, (3) USGS, U.S. Department of the Interior U.S. Geological Survey (2018). Focal mechanisms from C2011 are from waveform modeling unless otherwise stated. The reported nodal plane is the one favored by the stress inversion (i.e., the plane with the smallest misfit, the magnitude of which is also reported). We also indicate which mechanisms were filtered during the stress inversion. Map of focal mechanisms is given in Figure 1. gCMT; Global Centroid-Moment-Tensor Project.

The revised stress field shows a  $10^\circ$  clockwise rotation of  $\sigma_3$  to 10/072 relative to the Delvaux and Barth (2010) inversion (Figure 3). Notably, the new  $S_{hmin}$  (00/073) is now consistent with the extension directions from GPS stations in Malawi (Figure 1), and the azimuthal uncertainty has been reduced, from average  $\omega = \pm 21^\circ$  to  $\pm 12^\circ$ . This may reflect that Delvaux and Barth (2010) included all focal mechanisms in their inversion regardless of their compatibility, whereas our increased data set allowed a more selective approach. However, the uncertainty in this solution is too high (maximum horizontal stress,  $S_{Hmax}$ , azimuth one standard deviation uncertainty is  $\pm 22^\circ$ , Figure 3) to definitively exclude the possibility of E-W or NE-SW extension, or a heterogenous stress state in southern Malawi.

This inversion is also inconsistent with dip slip slickensides on NNE striking faults (Chorowicz & Sorlien, 1992; Wedmore et al., 2019). Stress inversions combining fault slickensides and earthquake focal mechanisms were performed; however, it was not possible to determine a reliable reduced stress tensor as either the data filtering was too severe or the stress shape ratio ( $\Phi = \sigma_2 - \sigma_3 / \sigma_1 - \sigma_3$ , where  $\sigma_2$  is the intermediate principal stress) indicated an unrealistic prolate stress ellipsoid ( $\Phi = 0.01 \pm 0.04$ , Lisle et al., 2006; Text S1 and Figure S3). Similarly, stress inversions using focal mechanisms from just southern Malawi resulted in stress inversions with  $\Phi = 0.13 \pm 0.09$  (Figure S4 and Text S2). Hence, there is a need to consider other indicators of stress within the rift and fault reactivation potential.

### 3.3. Joint Orientations

Figures 2 and 4 show the orientations of two steeply dipping mutually cross-cutting joint sets in southern Malawi, which strike N-S and E-W. Measurements were made in either Southern Irumide Belt basement rocks, which in this region comprise a range of charnockites, metasediments, and mafic paragneisses, or in Upper Jurassic-Late Cretaceous Chilwa Alkaline Province syenites and norites (Bloomfield, 1965; Dawson & Kirkpatrick, 1968; Dulanya, 2017; Manda et al., 2019; Manyozo et al., 1972). The observation of these joint sets in the latter suggests that they postdate Karoo extension, and a relatively young age is also supported by their open bare surfaces (Figure 4b), which imply formation without any precipitation or

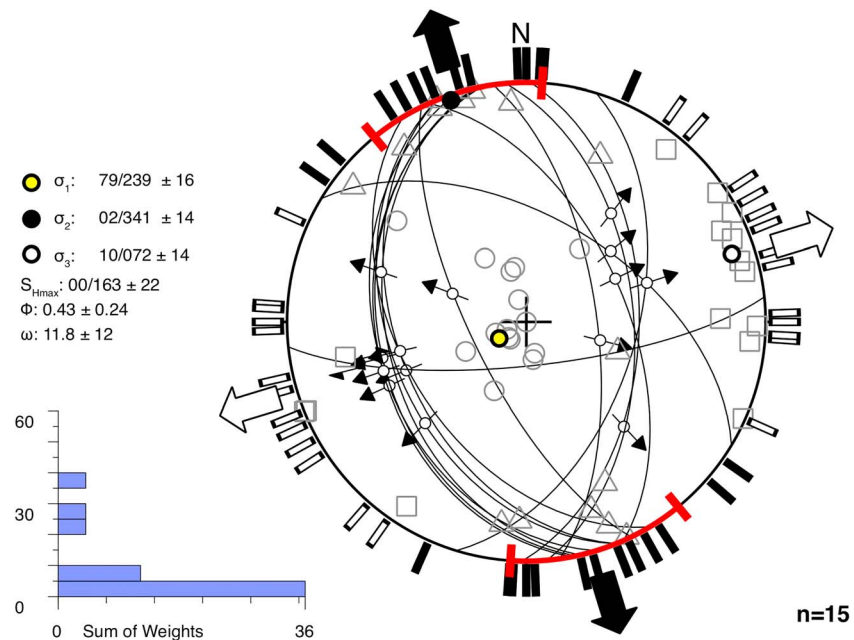


**Figure 3.** Results of earthquake focal mechanism stress inversion for the Malawi Rift using Win-Tensor (Delvaux & Sperner, 2003) and the mechanisms listed in Table 1. Lower-hemisphere equal area stereoplot depicts selected nodal planes (black lines) with slip vectors (black arrows), the three principal stress axes, maximum and minimum horizontal stress ( $S_{Hmax}$  and  $S_{Hmin}$ ) trajectories (black and white arrows outside stereoplot respectively), 1 standard deviation error bars for  $S_{Hmax}$  (red arc),  $S_{Hmax}$  and  $S_{Hmin}$  trajectories for individual focal mechanisms (black and white bars outside stereoplot), and kinematic axes for individual focal mechanisms (grey circle:  $p$  axis, triangle:  $b$  axis, square:  $t$  axis). Histogram represents distribution of misfit angles ( $\omega$ ), weighted arithmetically according to magnitude. One standard deviation of each parameter is also reported.

annealing processes that could be expected if the joints formed prior to exhumation. Joint orientations were all measured  $>50$  m from faults and are inferred to be outside their respective damage zones.

If it is hypothesized that the N-S striking joints are opening parallel to the trend of  $\sigma_3$ , it is possible to derive another estimate for the  $\sigma_3$  orientation within southern Malawi. To do this, we quantitatively analyze joint orientations using Kamb Contours (Figure 4a), where contours represent standard deviations away from the expected density of a random sample (Kamb, 1959). This analysis finds that the highest concentration of poles to the N-S striking joint set trends  $082^\circ \pm 7^\circ$ , which is taken here as the joint-derived  $\sigma_3$  trend. This trend indicates an extension direction that is within error of the extension direction for the Malawi Rift indicated by geodetic models (Saria et al., 2014; Stamps et al., 2018). The E-W striking joints are interpreted to reflect either an orthogonal joint set to the N-S set, and/or the emplacement of E-W striking Chilwa Akaline Province dykes (Bloomfield, 1965). Many of the N-S striking joints are foliation-parallel and thus may not reflect tectonic stresses (e.g., Engelder, 1985; Price, 1959; Williams et al., 2018). However, the N-S striking joint set is also observed within isotropic rocks. Thus, the  $\sigma_3$  trend ( $079^\circ \pm 8^\circ$ , Figure S5) is not significantly changed when foliation-parallel joints are removed from the analysis. This trend is also within error of the revised stress inversion (Figure 3).

#### 4. Fault Strength in Southern Malawi

To calculate fault reactivation potential at the southern end of the Malawi Rift, it is necessary to consider the frictional properties of its faults. We therefore selected three faults (Thyolo, Chingale Step, and Bilila-Mtakataka, Figure 2a), which (1) encompass the range of fault orientations in southern Malawi, (2) have prominent scarps and are therefore considered active (Hodge et al., 2018, 2019; Jackson & Blenkinsop, 1997; Wedmore et al., 2019), and (3) are well exposed, so it is possible to sample them for compositional analysis. The footwall of the Chingale Step and Thyolo faults consist of intensely fractured basement, which is in contact with hanging wall post-Miocene sediments across a  $<1$ -m thick fault gouge (Figure 5; Dulanya,

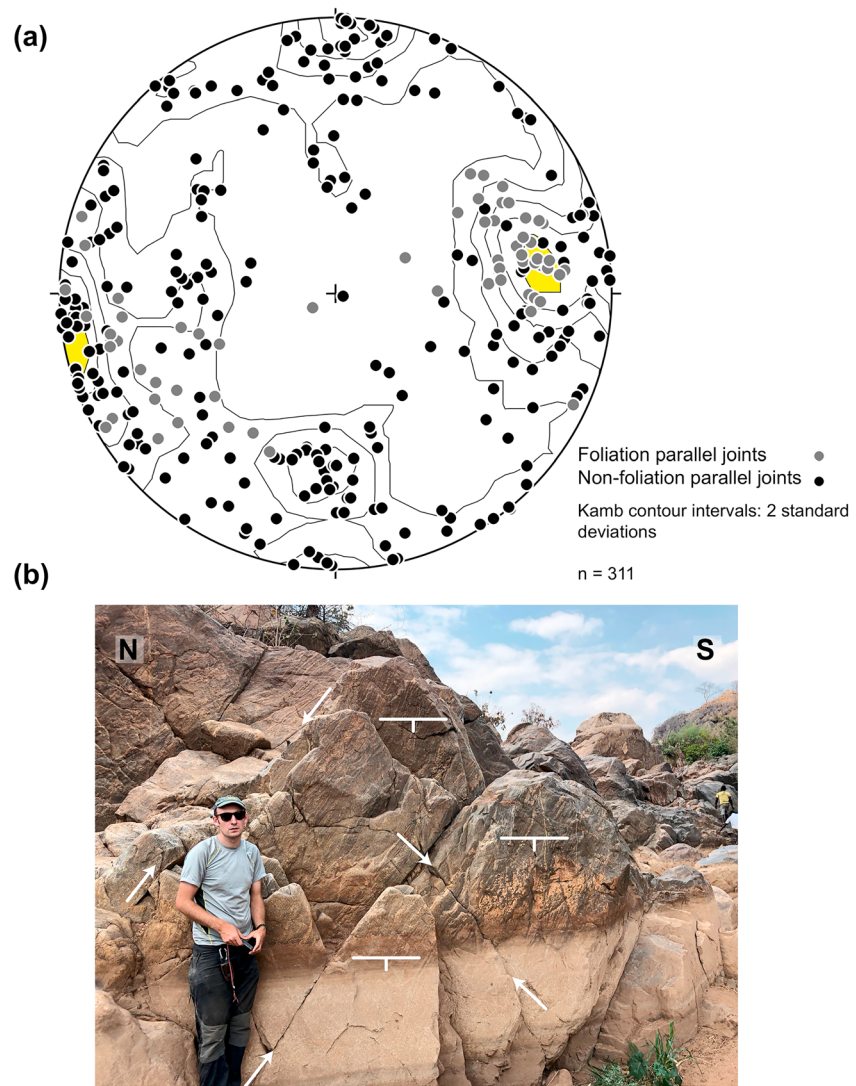


**Figure 4.** (a) Stereoplot showing poles to joint orientations that are also shown in Figure 2c. Shaded contour interval indicates highest concentration of the N-S striking joints. The trend at the center of this interval ( $082^\circ$ ) is used to infer the trend of the minimum principal stress ( $\sigma_3$ ) for Stress State 2. The range of this interval is  $\pm 7^\circ$ . (b) Examples of joint sets in the Malawi Rift. The joint set the facing the photo is a steeply dipping N-S set, which are mutually cross cutting with an inclined E-W set.

2017). Along most of its length, the Bilila-Mtakataka fault consists of a soil-mantled scarp (Hodge et al., 2018; Jackson & Blenkinsop, 1997). However, at Kasinje (Figure 2a), the fault consists of a 3-m thick unit of fractured gneiss that separates footwall and hanging wall hornblende gneisses (Hodge et al., 2018).

To assess fault zone composition, X-ray diffraction (XRD) analyses were conducted on two samples from each fault: (1) a “country rock” sample from the intact basement closest to the fault and (2) a “fault rock” sample from the faulted contact itself, that is, the fault gouge for the Thyolo and Chingale Step faults (Figure 5), and fractured gneiss for the Bilila-Mtakataka fault. XRD patterns were collected on powdered samples with a Philips PW1710 Automated Powder Diffractometer using Cu-K $\alpha$  radiation at 35 kV and 40 mA, between  $2$  and  $70^\circ$   $2\theta$ , at a scan speed of  $0.04^\circ$   $2\theta/s$ . From the scans, phases were identified using Philips PC Identify software. Using the peak areas, semiquantitative analysis was then performed to estimate the weight percentage of each identified phase (Table 2 and Figure S6).

For each fault, we find that the phyllosilicate content is typically  $<15\%$  (Table 2). This is significant as faults that are frictionally weak (fault static coefficient of friction  $[\mu_s] < 0.4$ ) typically contain interconnected

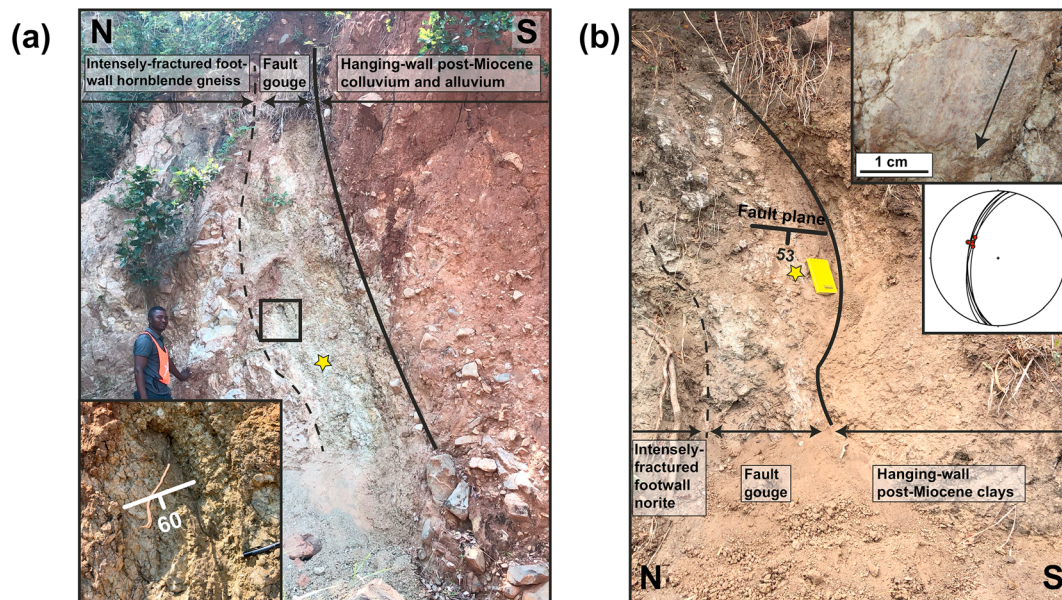


**Figure 5.** Examples of outcrops from the (a) Thyolo and (b) Chingale Step faults. Stars depict where “fault rock” samples were taken from for these faults. Footwall and hanging wall unit descriptions taken from Habgood et al. (1973) and Bloomfield (1965) respectively. Box in (a) highlights plane that was used to measure dip of Thyolo fault and is shown in the inset. Inset in (b) shows fault slickensides and orientations plotted on a lower hemisphere equal area stereonet (Wedmore et al., 2019). Note that a dip of 57° was used for the Chingale Step fault reactivation analysis, based on the average dip measured over other sites (Figure 2a).

phyllosilicates phases that constitute >30%–40% of the fault rock (Massironi et al., 2011; Moore & Lockner, 2004). Thus, we infer that these faults exhibit “Byerlee” frictional strengths ( $\mu_s \sim 0.6\text{--}0.8$ ; Byerlee, 1978), which is consistent with the results of deformation experiments on a suite of basement lithologies from the Malawi Rift ( $\mu_s = 0.55\text{--}0.80$ ; Hellebrekers et al., 2019). Differences in composition between country rock and fault rock samples are observed, such as for the Chingale Step fault, where calcite is dominant in the fault rock but is not detected in the country rock sample (Table 2). With these samples alone, however, we cannot determine if these differences reflect local protolith variations, near-surface weathering (Isaacs et al., 2007), or fault zone alteration (Sutherland et al., 2012).

### 5. Fault Reactivation Potential Analysis in Southern Malawi

Fault reactivation potential considers how susceptible a fault, of a given orientation and stress state, is to slip under the Mohr-Coulomb failure criterion. This criterion describes the shear stress ( $\tau$ ) required for a fault to exceed its frictional resistance (e.g., Sibson, 1985):

$$\tau = c + \mu_s(\sigma_n - P_f) \quad (1)$$

where  $\sigma_n$  is the normal stress,  $c$  is cohesive strength, and  $P_f$  is pore fluid pressure. We consider fault reactivation potential in southern Malawi in terms of stress ratio, slip tendency, and effective coefficient of friction (Figure 6).

**Table 2**  
Quantitative XRD (as Weight %) of Samples Collected From Fault Zones in the Malawi Rift

Fault	Sample	Quartz	Albite	Biotite	Muscovite	Actinolite	Kaolinite	Montmorillonite	Dolomite	Prehnite	Calcite
Thyolo	Country rock	43	40			14	3				
	Fault rock	81					8	5		6	
Chingale Step	Country rock	30	30	37			3				
	Fault rock	4						2	1		93
Bilila-Mtakataka	Country rock	11	52		8	26	3				
	Fault rock	74	16								10

*Note.* Results are normalized to 100% and so do not include estimates of unidentified or amorphous material. X-ray diffraction (XRD) diffractograms are given in Figure S6.

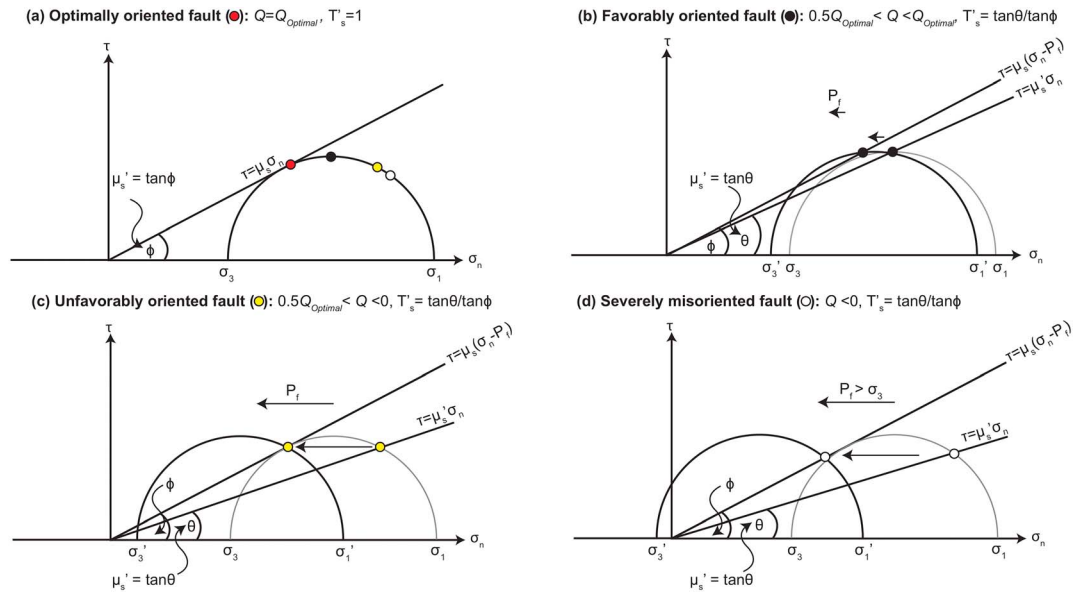


**Figure 6.** Illustration in Mohr Space of different concepts for analyzing fault reactivation. (a) The stress ratio ( $Q = \sigma_3/\sigma_1$ ), normalized slip tendency ( $T'_s$ ), and effective coefficient of friction ( $\mu'_s$ ) acting on an optimally oriented cohesionless fault. In this case,  $Q = Q_{Optimal}$ ,  $T'_s = 1$ ,  $\mu'_s$  is the same as the frictional strength of an optimally oriented fault ( $\mu_s = \tan\phi$ ), and no fluid pressure ( $P_f$ ) is required for reactivation. In addition, the orientation of three hypothetical faults is also depicted. The  $Q$ ,  $T'_s$ ,  $\mu'_s$ , and  $P_f$  required for reactivation of these (b) favorably oriented, (c) unfavorably oriented, and (d) severely misoriented fault is then also shown. For clarity, this example is for a 2-D reactivation analysis when the fault plane contains  $\sigma_2$ . However, the principles are the same for a 3-D analysis.

### 5.1. Stress Ratio

The stress ratio is the ratio between  $\sigma_3$  and  $\sigma_1$  required for fault slip ( $Q = \sigma_3/\sigma_1$ , Figure 6; Sibson, 1985). For the assessed faults, which do not necessarily contain  $\sigma_2$  in the stress states we consider, we use the 3-D solution outlined by Leclère and Fabbri (2013), where

$$Q = \frac{-(2AD\mu_s + 2C) \pm \sqrt{\Delta}}{A^2\mu_s^2 - C} \quad (2)$$

Here,  $A$ ,  $C$ ,  $D$ , and  $\Delta$  are functions defined by the stress shape ratio ( $\Phi$ ),  $c$ ,  $\mu_s$ , magnitude of  $\sigma_1$ , and the direction cosines between the normal to the fault plane and the three principal stress axes (see Text S3).

We calculate  $Q$  for the three faults described in section 4, given Stress States 1–3 (Figures 2d–2f). For Stress State 1 (NE-SW trending  $\sigma_3$ ) we use the principal stress orientations derived in the Delvaux and Barth (2010) stress inversion ( $\sigma_1 = 83/070$ ,  $\sigma_2 = 02/333$ ,  $\sigma_3 = 06/242$ ), for Stress State 2 (ENE-WSW trending  $\sigma_3$ ) the orientations derived in the new inversion ( $\sigma_1 = 79/239$ ,  $\sigma_2 = 02/341$ ,  $\sigma_3 = 10/072$ , Figure 3), and for Stress State 3 (E-W trending  $\sigma_3$ ) the orientations based on joint orientations ( $\sigma_1 = 90/000$ ,  $\sigma_2 = 00/172$ ,  $\sigma_3 = 00/082$ ). No reactivation analysis is conducted for the stress rotation hypothesis (Stress State 4, Morley, 2010), as it intrinsically assumes that all faults are favorably oriented for failure (i.e., Figure 6b).

The strike of the Chingale Step and Thyolo faults is constrained from their scarps that are visible in a 12-m resolution TanDEM-X digital elevation model (Hodge et al., 2019; Wedmore et al., 2019). For the Chingale Step fault, the strike is the orientation of the line that connects the two ends of its scarp, while for the segmented Thyolo fault, strike is the orientation of its longer northwestern section (Figure 2a). Dips of  $57^\circ$  and  $60^\circ$  for the Chingale Step and Thyolo faults were derived from field measurements (Figure 5). The deep structure of the Bilila-Mtakataka fault is best described by two subparallel segments, the longest of which is oriented  $156/46$  NE (Hodge et al., 2018). By using these averaged strike measurements, we reduce the influence of fault nonplanarity caused by near-surface topographic stresses on our analysis (Norris & Cooper, 1995). Furthermore, although there is uncertainty in how representative surface measurements of fault dip are, these measurements are similar to those inferred at depth from geophysical surveys and focal mechanisms in the Malawi Rift and elsewhere in the EARS ( $35$ – $70^\circ$ , Table 1; Kolawole et al., 2018; Lavayssière et al., 2019; Mortimer et al., 2007; Wheeler & Rosendahl, 1994).

As justified in section 4, we infer that these faults exhibit Byerlee frictional strengths, and so  $\mu_s = 0.7$ . A foliation-parallel preexisting fault would generally be considered cohesionless (Morley et al., 2004; Sibson, 1985). However, the high-grade metamorphic fabrics within the Malawi Rift are qualitatively observed to be cohesive (Figure 4b). Furthermore, the rift's geodetically derived extension rate ( $\sim 2$  mm/year; Saria et al., 2014) and EARS Western Branch seismicity  $b$  values ( $\leq 1$ ; Hodge et al., 2015; Lavayssière et al., 2019) both imply long recurrence intervals between earthquakes, so it is possible that interseismic healing has led to fault cohesion recovery (Tenthorey & Cox, 2006). To account for this ambiguity, we calculate  $Q$  for end-member cases where  $c = 0$  and  $c = 40$  MPa, the latter of which is derived from crystalline rocks typically exhibiting tensile strengths ( $T_0$ ) of 20 MPa, and that  $c \approx 2T_0$  (Lockner, 1995; Sibson, 1985, 1998).

No knowledge of stress magnitudes is required for calculating  $Q$  for a cohesionless fault (Leclère & Fabbri, 2013). However, the magnitude of  $\sigma_1$  is needed to determine  $Q$  for a cohesive fault, which is calculated by assuming an Andersonian normal fault stress state where

$$\sigma_1 = \sigma_v = \bar{\rho}(z)gz \quad (3)$$

where  $\sigma_v$  is the vertical stress,  $g$  is gravity ( $9.8 \text{ ms}^{-2}$ ),  $z$  is depth, and  $\bar{\rho}(z)$  is the average density of the overlying crust for a given depth, which is a function of an inferred Malawi Rift three-layer crustal model (Table S2; Nyblade & Langston, 1995; Fagereng, 2013). We initially assume the crust is dry, and so the pore fluid pressure,  $P_f = 0$ ; however, the influence of fluids on fault reactivation is discussed in sections 5.3 and 7. The stress shape ratio ( $\Phi$ ) is 0.43, as derived from the updated stress inversion (Figure 3).

### 5.2. Slip Tendency

Slip tendency ( $T_s$ ) is a measure of the ratio of  $\tau$  to  $\sigma_n$  acting on the fault surface (Lisle & Srivastava, 2004; Morris et al., 1996):

$$T_s = \frac{\tau}{\sigma_n} \quad (4)$$

For a given stress state, there is a maximum value of  $T_s$ , which is that acting on a cohesionless optimally oriented fault (Figure 6; Lisle & Srivastava, 2004). This leads to a normalized index of slip tendency ( $T'_s$ ) that ranges between 0 and 1:

$$T'_s = \frac{T_s}{\max(T_s)} = \frac{\tau}{\sigma_n \tan \phi} \quad (5)$$

(corrected from equation (3) in Lisle and Srivastava (2004); R. Lisle, personal communication, January 4, 2019) where  $\phi$  is the angle of internal fault friction ( $\tan \phi = \mu_s$ ). To calculate  $T_s$  and  $T'_s$  for the Chingale Step, Thyolo and Bilila-Mtakataka faults without knowledge of the magnitudes of  $\tau$  and  $\sigma_n$ , we use the solutions outlined by Lisle and Srivastava (2004); see Text S4. This analysis is performed for Stress States 1–3, assuming  $\mu_s = 0.7$ ,  $P_f = 0$ , and  $\Phi = 0.43$ .

### 5.3. Fault Effective Coefficient of Friction

The concept of  $T_s$  can be extended to calculate the effective coefficient of friction ( $\mu_s'$ ), which describes the maximum value of  $\mu_s$  or lowest value of  $P_f$  that allows faults to reactivate for a given stress state, without also inducing failure along optimally oriented planes in intact rock (Figure 6; Sibson, 1985; Muluneh et al., 2018). Like  $T_s$ ,  $\mu_s'$  is a measure of the ratio of  $\tau$  to  $\sigma_n$  acting on a fault; however, it is derived using inferred principal stress magnitudes, and fault cohesion can be incorporated. This is advantageous as  $\mu_s'$  can then be compared to values of  $\mu_s$  inferred from experimental and compositional analysis of faults to determine if they will reactivate in a given stress state, or if elevated fluid pressures are required.

Principal stress magnitudes can be derived as  $\mu_s'$  is being equated to the stresses acting on an optimally oriented fault (Figure 6), thus under Mohr-Coulomb theory (Jaeger et al., 2007):

$$\sigma_1 = 2c \sqrt{\frac{1 + \sin \phi_i}{1 - \sin \phi_i}} + \sigma_3 \left( \frac{1 + \sin \phi_i}{1 - \sin \phi_i} \right) \quad (6)$$

where  $\phi_i = \tan^{-1} \mu_i$  and  $\mu_i$  is the frictional strength of intact rock. Given the results of Hellebrekers et al. (2019),  $\mu_i = 0.7$ ; thus,  $\phi_i = 35^\circ$ . Since  $\sigma_1$  can be derived from equation (3), it is thus also possible to

**Table 3**

Results of Fault Reactivation Analysis in Terms of the Stress Ratio ( $Q$ ), Slip Tendency ( $T_s$ ), Normalized Slip Tendency ( $T'_s$ ), and Effective Frictional Strength ( $\mu'_s$ ) Needed to Reactivate Each Fault in Stress States 1–3

Stress State	Fault	Stress ratio ( $Q$ )				Slip tendency ( $T_s$ )	Normalized slip tendency ( $T'_s$ )	Effective coefficient of friction ( $\mu'_s$ )	
		$c = 0$	Class	$c = 40$ MPa	Class			$c = 0$	$c = 40$ MPa
1: $\sigma_3 = 06/242$	Thyolo	0.24	F	0.16	F	0.65	0.92	0.87	0.68
	Chingale Step	0.02	U	-0.08	S	0.43	0.62	0.55	0.42
	Bilila-Mtakataka	0.24	F	0.16	F	0.65	0.93	0.69	0.56
2: $\sigma_3 = 10/072$	Thyolo	0.24	F	0.16	F	0.62	0.88	0.81	0.64
	Chingale Step	0.19	F	0.11	U	0.56	0.81	0.65	0.50
	Bilila-Mtakataka	0.01	U	-0.09	S	0.45	0.65	0.69	0.56
3: $\sigma_3 = 00/082$	Thyolo	0.22	F	0.13	F	0.60	0.86	0.74	0.58
	Chingale Step	0.21	F	0.12	F	0.59	0.85	0.72	0.57
	Bilila-Mtakataka	0.17	F	0.08	U	0.56	0.80	0.66	0.54

Note. F = favorably oriented fault ( $Q > 0.5Q_{\text{Optimal}}$ ); U = unfavorably oriented fault ( $0.5Q_{\text{Optimal}} < Q < 0$ ), and S = severely misoriented fault ( $Q < 0$ , Figure 6; Leclère & Fabbri, 2013; Sibson, 1985).  $T_s$ ,  $T'_s$ , and  $Q$  where  $c = 0$  pertain to any depth.  $Q$  where  $c = 40$  MPa and  $\mu'_s$  are for a depth of 20-km and assume a fault surrounded by intact rock where  $\mu_i = 0.7$ . See Figures 7 and S9 for how these values vary with depth. All results to 2 decimal places.

calculate  $\sigma_3$  and  $\sigma_2$  by rearranging equation (6) and the equation for  $\Phi$  (equation (S1)), respectively. The principal stress magnitudes can then be used to calculate  $\tau$  and  $\sigma_n$  as a function of depth (Jaeger et al., 2007), and  $\mu'_s$  can be derived by rearranging the Mohr Coulomb criterion (equation (1)). Thus, for the parameters assumed here:

$$\mu'_s(z) = \frac{\sqrt{C \left( \frac{2.7z\bar{\rho}(z)-42}{9.8z\bar{\rho}(z)} \right)^2 - 2C \left( \frac{2.7z\bar{\rho}(z)-42}{9.8z\bar{\rho}(z)} \right) + C - \frac{c}{\sigma_1}}}{A \left( \frac{2.7z\bar{\rho}(z)-42}{9.8z\bar{\rho}(z)} \right) + B} \quad (7)$$

where the functions  $A$ ,  $B$ , and  $C$  are defined by equations (S2)–(S4) (see Texts S3 and S5). As previously, we calculate  $\mu'_s$  for the Thyolo, Chingale Step, and Bilila-Mtakataka faults being reactivated in Stress States 1–3; however, for Stress States 1 and 2, the principal stress axes are slightly rotated so that  $\sigma_1 = \sigma_v$ , and  $\sigma_2$  and  $\sigma_3$  equal  $S_{\text{Hmax}}$  and  $S_{\text{Hmin}}$ , respectively. This analysis considers both cohesionless and cohesive faults and is performed over a depth range of 6–35 km, which encompasses the range of earthquake nucleation in the Malawi Rift (Biggs et al., 2010; Craig et al., 2011; Nyblade & Langston, 1995).

The minimum pore fluid pressure ( $P_f$ ) required to reactivate a fault (Figure 6) can also be calculated as a function of depth,  $\mu_i$ , and  $\mu'_s$ :

$$P_f'(z) = \sigma_n(z) - \frac{\sigma_n(z)\mu'_s(z)}{\mu_i} \quad (8)$$

(see Text S5). This is calculated with  $\mu_i = 0.7$  and is plotted in terms of the effective pore-fluid factor ( $\lambda'_v = P_f'/\sigma_v$ ). For comparison, the orientation of the faults is also shown in a stereoplot that is contoured by  $\mu'_s$  values for each stress state for a given  $\Phi$ ,  $\mu_i$ , and depth. Plots of the maximum  $\mu'_s$  that allows all three faults to reactivate for all possible  $\sigma_3$  trends are also included. As fault reactivation is also influenced by variations in  $\Phi$  and  $\mu_i$  (Boulton et al., 2018), we show  $\mu'_s$  contour plots in  $\Phi$ - $\mu_i$  space for a fixed set of fault and principal stress orientations. In addition, the results of this analysis at a depth of 20 km are shown in 3-D Mohr Space using MohrPlotter v. 2.8.3 (Allmendinger et al., 2011).

## 6. Fault Reactivation Potential Results

The Thyolo and Bilila-Mtakataka faults have a high reactivation potential under Stress State 1, as their  $Q$  value is “favorable” and  $T'_s \sim 1$  (Table 3). Thus, they will reactivate under Stress State 1 at relatively high  $\mu'_s$  (>0.55), regardless of whether they are cohesive or not (Table 3 and Figures 7a, 8a, 9a, S7 and S9). Conversely, the Chingale Step fault is “unfavorably” to “severely misoriented” in this stress state (Table 3), depending on depth and whether it is cohesive.  $T'_s = 0.62$ , and at depths >10 km, it will not reactivate in Stress State 1 unless  $\mu_s < 0.6$  or  $\lambda_v > 0.1$  (Table 3 and Figures 8a, 9, S9a, and S10).

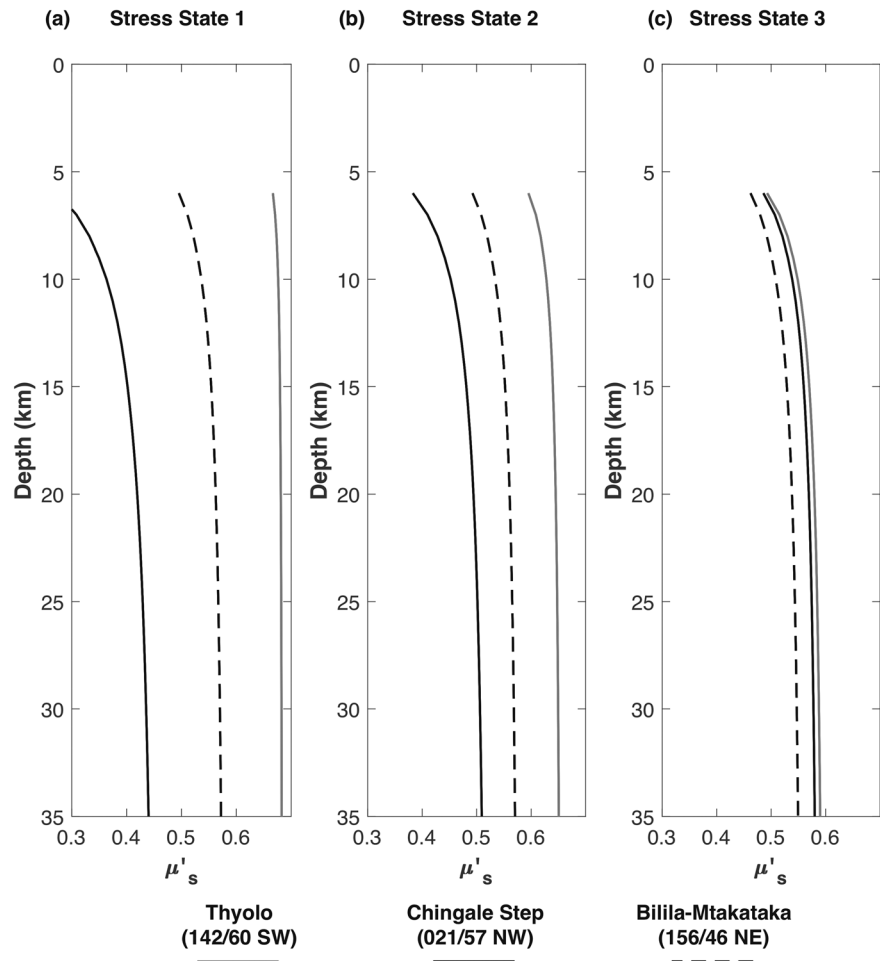


**Figure 7.** The effective coefficient of friction ( $\mu'_s$ ) required to reactivate the Thylo, Chingale Step, and Bilila-Mtakataka fault in (a–c) Stress States 1–3 between depths 6–35 km. Analysis for cohesive faults ( $c = 40$  MPa), with no fluid pressure, intact rock strength  $\mu_i = 0.7$ , and stress shape ratio  $\Phi = 0.43$ , and density model in Table S2. For equivalent figures for cohesionless faults, see Figure S9.

In Stress State 3, all faults exhibit  $T'_s > 0.8$ , although the reactivation potentials of the Thylo and Bilila-Mtakataka faults are slightly less than under Stress State 1 (Table 3). Therefore, all faults will reactivate at  $\mu'_s > 0.54$  at depths  $>10$  km (Table 3 and Figures 7c, 8c, 9d, and S9c). Fault reactivation potential in Stress State 2 is intermediate between Stress States 1 and 3 except for the Bilila-Mtakataka fault Q and  $T'_s$  analysis (Table 3 and Figure 7b, 8b, and S9b). This likely reflects the nonvertical plunge of  $\sigma_1$  obtained in this inversion (Figure 3), since intermediate values are observed when  $\sigma_1$  is assumed to be vertical for the  $\mu'_s$  calculations. All results for  $\mu'_s$  are broadly independent of the values of  $\Phi$  and  $\mu_i$  (Figures 10 and S11).

### 7. How Do Faults in Southern Malawi Reactivate?

An active fault scarp has been described along Chingale Step fault by Wedmore et al. (2019), and so its orientation is representative of a structure currently accommodating extension. However, if it is cohesionless at 10- to 35-km depth, in Stress State 1  $\mu'_s$  is between 0.50 and 0.60 (Figures 9b and S9a). This is at the lower end of frictional strengths inferred from its composition (Table 2) and deformation experiments on basement rocks in Malawi (Hellebrekers et al., 2019). In the cohesive fault case,  $\mu'_s = 0.35$ – $0.45$  (Figure 7a, 8a, and 8d), and so below its likely frictional strength.

Alternatively, the Chingale Step fault may reactivate under Stress State 1 at  $\mu'_s = 0.7$  through a moderate increase in fluid pressure ( $\lambda'_v = 0.1$ – $0.3$ , Figures 9c and S10), which is sustainable in a normal fault stress

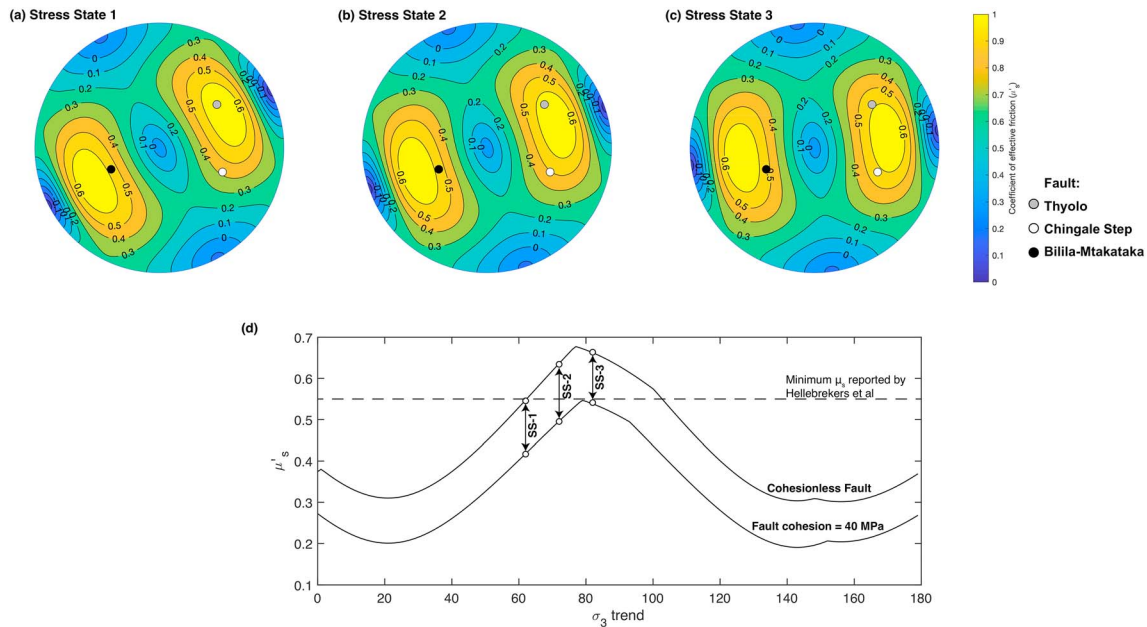


**Figure 8.** (a–c) Stereoplots contoured by the effective coefficient of friction ( $\mu'_s$ ) required to reactivate a cohesive fault ( $c = 40$  MPa) of any orientation in Stress States 1–3. Poles to the fault orientations analyzed here are also shown. Equivalent plots for a cohesionless fault are shown in Figure S7. (d) The maximum  $\mu'_s$  in which all three faults analyzed here reactivate as a function of  $\sigma_3$  trend. SS-1, SS-2, and SS-3 mark points where Stress States 1–3 plot respectively. Horizontal line represents lowest  $\mu'_s$  of basement rocks in Malawi reported by Hellebrekers et al. (2019). All results for a depth of 20 km, assuming the density model in Table S2, and that  $\sigma_2$  and  $\sigma_3$  equal  $S_{Hmax}$  and  $S_{Hmin}$ , respectively. For all plots the intact rock strength  $\mu_i = 0.7$ , stress shape ratio  $\Phi = 0.43$ , and there is no fluid pressure. Stereoplots constructed using Cardozo in Allmendinger et al. (2011).

state (Sibson & Rowland, 2003). However, post-Miocene hanging wall sediments are <100-m thick in southern Malawi (Bloomfield & Garson, 1965; Mynatt et al., 2017; Walshaw, 1965), so these faults juxtapose basement rocks across most of the crust. Given that these rocks have been dehydrated during one or more episodes of high grade metamorphism (Fagereng, 2013), fluid ingress into these fault zones is likely to be

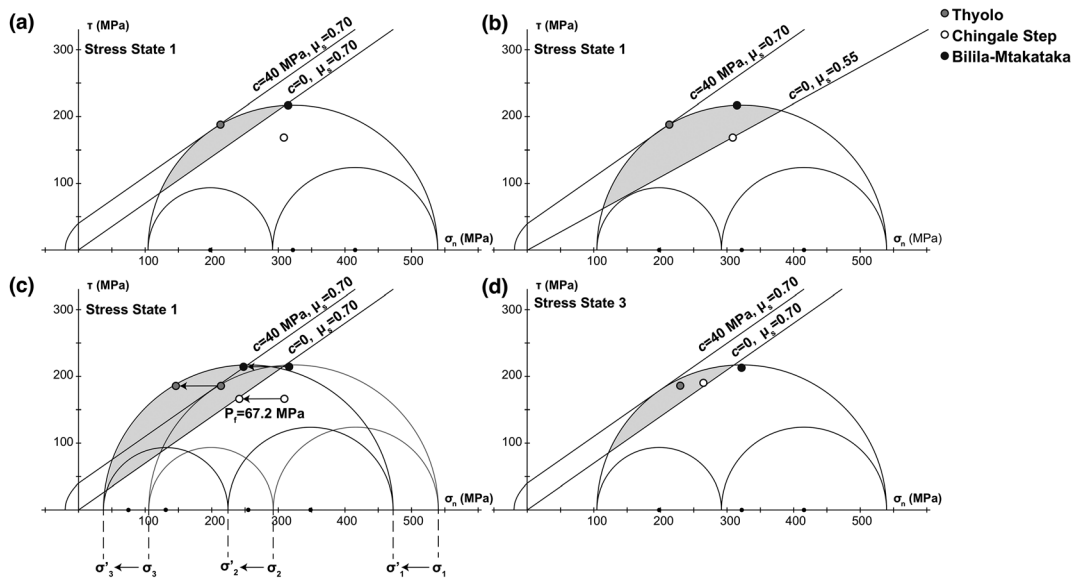


**Figure 9.** Three-dimensional Mohr Circle analysis for fault reactivation in southern Malawi at 20-km depth. Shaded region in each plot depicts range of orientations where a cohesionless fault will reactivate. (a) Orientation of Thyolo, Chingale Step and Bilila-Mtakataka Fault in Stress States 1. Given the failure criterions assumed here, only the Thyolo and Bilila-Mtakataka fault will reactivate. Reactivation of the Chingale Step fault instead requires that (b)  $\mu'_s = 0.55$  or that (c)  $P_f = 67.2$  MPa (equivalent to  $\lambda'_v = 0.12$ ). (d) Same as (a) but for Stress State 3. The Thyolo and Chingale Step faults will reactivate in this stress state, and reactivation of Bilila-Mtakataka requires a slight reduction in  $\mu'_s$  to 0.66 (Table 3). Analysis assumes  $\Phi = 0.43$  and density model in Table S2.

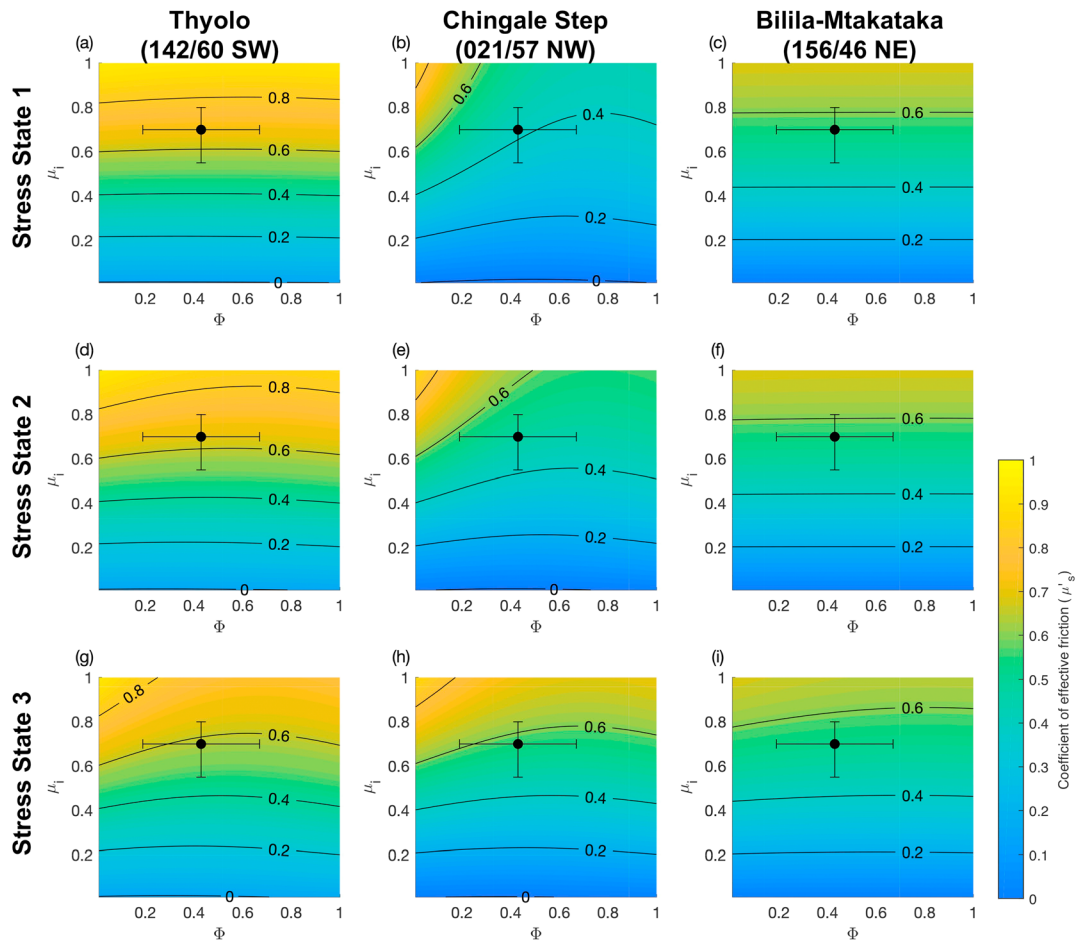


**Figure 10.** Contour plots for effective coefficient of friction ( $\mu_s'$ ) needed for reactivation of a cohesive fault ( $c = 40$  MPa) in intact rock frictional strength-stress shape ratio ( $\mu_i$ - $\Phi$ ) space for the given fault orientations and Stress States 1–3 at 20-km depth. Black circle represents point where  $\Phi = 0.43$  and  $\mu_i = 0.70$ , as used in Figure 7, with error bars representing range of  $\mu_i$  reported by Hellebrekers et al. (2019;  $\mu_i = 0.55$ – $0.80$ ), and 1 standard deviation uncertainty in  $\Phi$  ( $0.43 \pm 0.24$ ). For similar analysis for cohesionless fault, see Figure S10.

limited (Hollinsworth et al., 2019). Indeed, even in northern Malawi where sediments are ~500-m thick (Kolawole et al., 2018), there is little fluid involvement in active faulting (Gaherty et al., 2019). Low fluid pressures around these faults is also illustrated by the lack of extensive vein networks observed in their damage zones (Figure 5; cf. Bruhn et al., 1994; Caine et al., 2010; Sutherland et al., 2012).

This reactivation analysis cannot definitively discount stress states; ideally, these should be measured using a range of techniques (e.g., borehole breakouts). Nevertheless, it does suggest that previous models of a NW-SE trending  $\sigma_3$  in Malawi (Chorowicz & Sorlien, 1992; Mortimer et al., 2007; Ring et al., 1992) would require unreasonably weak faults ( $\mu_s' < 0.5$ , Figure 8d). Furthermore, it is difficult to account for why a structure with the NNE-SSW strike of the Chingale Step fault would have activated and continue reactivating in Stress State 1, instead of a more optimally oriented fault forming. Conversely, in Stress States 2 and 3, all faults can reactivate at  $\mu_s$  or  $P_f$  that require neither frictionally weak minerals nor elevated fluid pressure (Figures 7–9). In addition, fault slickensides in the Zomba Graben (Figure 5; Chorowicz & Sorlien, 1992; Wedmore et al., 2019) indicate NW-SE extension, in contrast to the highly oblique ( $\alpha < 40^\circ$ ) NE-SW extension predicted by applying the Wallace-Bott criterion to Stress State 1. Indeed, it is difficult to reconcile any uniform stress state to the range of NW-SE to NE-SW extension directions that have been proposed for the Malawi Rift based on fault slickensides and earthquake focal mechanisms (see section 3.1).

A range of extension directions could be accounted for by the model proposed in Morley (2010) whereby Southern Irumide metamorphic fabrics rotate  $\sigma_3$  along the rift, so that all faults are dip slip (i.e., Stress State 4, Figure 2g). In this way, all faults will be favorably oriented for reactivation. Furthermore,

although some oblique slip focal mechanisms (Table 1) and fault slickensides are recorded in southern Malawi, in the former case, these tend to be historical focal mechanisms that were not instrumentally well recorded, while with regard to the latter, this may relate to slickensides that record the inherent oblique slip component of normal faulting earthquakes as the fault tip is approached (Hampel et al., 2013; Philippon et al., 2015; Roberts, 1996). There is, however, a discrepancy between Stress State 4 and the homogenous orientation of joint sets in southern Malawi, which suggest a uniform stress state (Figures 2 and 4). The Bilila-Mtakataka and Chingale Step faults also locally crosscut the foliation in a nonsystematic manner at the surface (Figure 2a; Bloomfield, 1965; Jackson & Blenkinsop, 1997; Hodge et al., 2018), further suggesting that the foliation is not actively rotating stresses.

We therefore propose a variation of the Morley (2010) hypothesis that is based on analog models (Corti et al., 2013; Philippon et al., 2015) and which satisfies the constraints of variably striking frictionally strong normal faults and consistently oriented joints sets. Here, the regional principal stress axes (*sensu* Pollard et al., 1993) in southern Malawi are uniform but local fault slip vectors (in the sense of Twiss & Unruh, 1998) are rotated to dip slip along the rift by a deep-seated weak ductile shear zone that is oblique to  $\sigma_3$ , but which conditions the kinematics, geometry, and distribution of the rift's faults (Hodge et al., 2018; Wedmore et al., 2019). Our reactivation analysis indicates that a uniform  $\sigma_3$  in southern Malawi should trend between ENE-WSW (Stress State 2) and E-W (Stress State 3; Figures 7 and 8). If true, this hypothesis has the following implications:

1. A polymodal range of fault orientations at the southern end of the Malawi Rift (Figure 2a) can be accounted for by a uniform stress state and the Mohr Coulomb criterion, given variably oriented pre-existing crustal weaknesses (*cf.* Healy et al., 2015).
2. NW and NNE striking faults in southern Malawi do not represent a sequential set of highly oblique faults that link faults striking orthogonal to  $\sigma_3$ . Instead, all faults reactivate while striking slightly oblique ( $\alpha > 50^\circ$ ) to a uniformly trending  $\sigma_3$  (Figures 2e and 2f).
3. Using fault slickensides and earthquake focal mechanisms in stress inversions is problematic as regional stresses and local incremental fault displacements are not necessarily aligned (Philippon et al., 2015; Twiss & Unruh, 1998). Furthermore, accurate principal stress directions will not be derived from stress inversions in which only a subset of fault orientations from a polymodal distribution are included (Healy et al., 2015; Twiss & Unruh, 1998).
4. This justifies a reassessment of the stress states that have been inferred elsewhere in the Malawi Rift (Chorowicz & Sorlien, 1992; Delvaux & Barth, 2010; Mortimer et al., 2007; Ring et al., 1992), and other rifts where highly oblique transfer zones have been proposed (e.g., Acocella et al., 1999; Chorowicz & Deffontaines, 1993).
5. Normal faults with a wide range of strikes can all reactive within the same stress state, which should be considered when assessing seismic hazard in continental rifts.

## 8. Conclusions

Previous studies have proposed NE-SW, ENE-WSW, E-W, and SE-NW extension directions in the Malawi Rift. Here, we demonstrate how the reactivation potential of three variably striking active faults supports a  $\sigma_3$  trend in southern Malawi that lies between ENE-WSW and E-W (Figure 8). Previous estimates of a NW-SE (Chorowicz & Sorlien, 1992; Delvaux, 2001; Mortimer et al., 2007; Ring et al., 1992) or NE-SW  $\sigma_3$  trend (Delvaux et al., 2012; Delvaux & Barth, 2010) are considered unlikely as they require that some faults in the rift are highly oblique and thus reactivate with unreasonably low frictional strengths and/or high pore fluid pressures. Furthermore, an ENE-WSW to E-W  $\sigma_3$  trend is consistent with regional joint sets (Figures 2 and 4), an updated focal mechanism stress inversion (Figure 3), and geodetic data (Stamps et al., 2018). An alternative hypothesis that foliation actively rotates the stresses along the rift (Stress State 4, Figure 2f; Morley, 2010) is inconsistent with spatially homogeneous joint orientations and local variations in the foliation orientation.

An ENE-WSW to E-W  $\sigma_3$  trend suggests that all faults in southern Malawi reactivate at slightly oblique angles (angle between fault strike and regional  $\sigma_3$  trend  $>50^\circ$ ) and thus counter to typical models of oblique rifting in which one fault set strikes orthogonal to  $\sigma_3$  and the other is highly oblique (e.g., Acocella et al., 1999; McClay & White, 1995). It is unclear whether this slightly oblique extension is reflected in the

kinematics of faults in southern Malawi, or if the faults are actually pure dip slip as indicated by the few well-determined focal mechanisms (Table 1). In the latter case, this can be explained by a deep-seated zone of crustal weakness, which reorients slip (Corti et al., 2013; Hodge et al., 2018; Philippon et al., 2015). Either way, in rifts where stress states derived from measurements of incremental fault displacement are ambiguous, fault reactivation potential analysis provides a powerful way to test their applicability.

#### Acknowledgments

This research was funded by the EPSRC Global Challenges Research Fund (grant EP/P028233/1 "PREPARE"). TANDEM-X data were obtained via DLR proposal DEM\_GEOL0686. Henri Leclère and Carolyn Boulton are thanked for providing codes to calculate the stress ratio of faults and guidance on how to use them. Antony Oldroyd conducted the XRD analysis and interpretation. We thank Cindy Ebinger and two anonymous reviewers for their constructive comments. All data are included in the main text or supporting information.

#### References

- Acocella, V., Faccenna, C., Funicello, R., & Rossetti, F. (1999). Sand-box modelling of basement-controlled transfer zones in extensional domains. *Terra Nova*, *11*(4), 149–156. <https://doi.org/10.1046/j.1365-3121.1999.00238.x>
- Aldrich, M. J. (1986). Tectonics of the Jemez lineament in the Jemez Mountains and Rio Grande Rift (USA). *Journal of Geophysical Research*, *91*(B2), 1753. <https://doi.org/10.1029/JB091iB02p01753>
- Allmendinger, R. W., Cardozo, N., & Fisher, D. M. (2011). *Structural geology algorithms: Vectors and tensors*. Cambridge: Cambridge University Press. <https://doi.org/10.1017/CBO9780511920202>
- Andreoli, M. A. G. (1984). Petrochemistry, tectonic evolution and metasomatic mineralisations of Mozambique belt granulites from S Malawi and Tete (Mozambique). *Precambrian Research*, *25*(1–3), 161–186. [https://doi.org/10.1016/0301-9268\(84\)90031-7](https://doi.org/10.1016/0301-9268(84)90031-7)
- Angelier, J., & Mechler, P. (1977). Sur une méthode graphique de recherche des contraintes principales également utilisable en tectonique et en séismologie: La méthode des dièdres droits. *Bulletin de La Société Géologique de France*, *7*(6), 1309–1318. <https://doi.org/10.2113/gssgfbull.S7-XIX.6.1309>
- Bellahsen, N., Fournier, M., D'Acromont, E., Leroy, S., & Daniel, J. M. (2006). Fault reactivation and rift localization: Northeastern Gulf of Aden margin. *Tectonics*, *25*, TC1007. <https://doi.org/10.1029/2004TC001626>
- Biggs, J., Nissen, E., Craig, T., Jackson, J., & Robinson, D. P. (2010). Breaking up the hanging wall of a rift-border fault: The 2009 Karonga earthquakes, Malawi. *Geophysical Research Letters*, *37*, L11305. <https://doi.org/10.1029/2010GL043179>
- Bloomfield, K. (1958). The geology of the Port Herald Area. Bulletin of the Geological Survey, Malawi, 9.
- Bloomfield, K. (1965). The geology of the Zomba Area. Bulletin of the Geological Survey, Malawi, 16.
- Bloomfield, K., & Garson, M. S. (1965). The geology of the Kirk Range-Lisungwe Valley area. Bulletin of the Geological Survey, Malawi, 17.
- Bott, M. H. P. (1959). The mechanics of oblique slip faulting. *Geological Magazine*, *96*(2), 109–117. <https://doi.org/10.1017/S0016756800059987>
- Boulton, C., Barth, N. C., Moore, D. E., Lockner, D. A., Townend, J., & Faulkner, D. R. (2018). Frictional properties and 3-D stress analysis of the southern Alpine Fault, New Zealand. *Journal of Structural Geology*, *114*, 43–54. <https://doi.org/10.1016/j.jsg.2018.06.003>
- Bruhn, R. L., Parry, W. T., Yonkee, W. A., & Thompson, T. (1994). Fracturing and hydrothermal alteration in normal fault zones. *Pure and Applied Geophysics*, *142*(3–4), 609–644. <https://doi.org/10.1007/BF00876057>
- Brune, S. (2014). Evolution of stress and fault patterns in oblique rift systems: 3-D numerical lithospheric-scale experiments from rift to breakup. *Geochemistry, Geophysics, Geosystems*, *15*, 3392–3415. <https://doi.org/10.1002/2014GC005446>
- Byerlee, J. D. (1978). Friction of rocks. *Pure and Applied Geophysics PAGEOPH*, *116*(4–5), 615–626. <https://doi.org/10.1007/BF00876528>
- Caine, J. S., Bruhn, R. L., & Forster, C. B. (2010). Internal structure, fault rocks, and inferences regarding deformation, fluid flow, and mineralization in the seismogenic Stillwater normal fault, Dixie Valley, Nevada. *Journal of Structural Geology*, *32*(11), 1576–1589. <https://doi.org/10.1016/j.jsg.2010.03.004>
- Castaing, C. (1991). Post-Pan-African tectonic evolution of South Malawi in relation to the Karroo and recent East African rift systems. *Tectonophysics*, *191*(1–2), 55–73. [https://doi.org/10.1016/0040-1951\(91\)90232-H](https://doi.org/10.1016/0040-1951(91)90232-H)
- Chorowicz, J., & Deffontaines, B. (1993). Transfer faults and pull-apart model in the rhinegraben from analysis of multisource data. *Journal of Geophysical Research*, *98*(B8), 14,339–14,351. <https://doi.org/10.1029/93JB00190>
- Chorowicz, J., & Sorlien, C. (1992). Oblique extensional tectonics in the Malawi Rift, Africa. *Geological Society of America Bulletin*, *104*(8), 1015–1023. [https://doi.org/10.1130/0016-7606\(1992\)104<1015:OETITM>2.3.CO;2](https://doi.org/10.1130/0016-7606(1992)104<1015:OETITM>2.3.CO;2)
- Corti, G. (2012). Evolution and characteristics of continental rifting: Analog modeling-inspired view and comparison with examples from the East African Rift System. *Tectonophysics*, *522*–523, 1–33. <https://doi.org/10.1016/j.tecto.2011.06.010>
- Corti, G., Philippon, M., Sani, F., Keir, D., & Kidane, T. (2013). Re-orientation of the extension direction and pure extensional faulting at oblique rift margins: Comparison between the Main Ethiopian Rift and laboratory experiments. *Terra Nova*, *25*(5), 396–404. <https://doi.org/10.1111/ter.12049>
- Craig, T. J., Jackson, J. A., Priestley, K., & McKenzie, D. (2011). Earthquake distribution patterns in Africa: Their relationship to variations in lithospheric and geological structure, and their rheological implications. *Geophysical Journal International*, *185*(1), 403–434. <https://doi.org/10.1111/j.1365-246X.2011.04950.x>
- Dawson, A. L., & Kirkpatrick, I. M. (1968). The geology of the Cape Maclear peninsula and Lower Bwanje valley. Bulletin of the Geological Survey, Malawi, 28.
- Delvaux, D. (2001). Tectonic and palaeostress evolution of the Tanganyika-Rukwa-Malawi rift segment, East African Rift System. Peri-Tethys Memoir 6: Peri-Tethyan Rift/Wrench Basins and Passive Margins, 545–567.
- Delvaux, D., & Barth, A. (2010). African stress pattern from formal inversion of focal mechanism data. *Tectonophysics*, *482*(1–4), 105–128. <https://doi.org/10.1016/j.tecto.2009.05.009>
- Delvaux, D., Kervyn, F., Macheyeke, A. S., & Temu, E. B. (2012). Geodynamic significance of the TRM segment in the East African Rift (W-Tanzania): Active tectonics and paleostress in the Ufipa plateau and Rukwa basin. *Journal of Structural Geology*, *37*, 161–180. <https://doi.org/10.1016/j.jsg.2012.01.008>
- Delvaux, D., & Sperner, B. (2003). New aspects of tectonic stress inversion with reference to the TENSOR program. *Geological Society, London, Special Publications*, *212*(1), 75–100. <https://doi.org/10.1144/GSL.SP.2003.212.01.06>
- Dulanya, Z. (2017). A review of the geomorphotectonic evolution of the south Malawi rift. *Journal of African Earth Sciences*, *129*, 728–738. <https://doi.org/10.1016/j.jafrearsci.2017.02.016>
- Ebinger, C. J. (1989). Tectonic development of the western branch of the East African rift system. *Geological Society of America Bulletin*, *101*(7), 885–903. [https://doi.org/10.1130/0016-7606\(1989\)101<0885:TDOTWB>2.3.CO;2](https://doi.org/10.1130/0016-7606(1989)101<0885:TDOTWB>2.3.CO;2)
- Ebinger, C. J., Rosendahl, B. R., & Reynolds, D. J. (1987). Tectonic model of the Malawi rift, Africa. *Tectonophysics*, *141*(1–3), 215–235. [https://doi.org/10.1016/0040-1951\(87\)90187-9](https://doi.org/10.1016/0040-1951(87)90187-9)

- Eby, G. N., Roden-Tice, M., Krueger, H. L., Ewing, W., Faxon, E. H., & Woolley, A. R. (1995). Geochronology and cooling history of the northern part of the Chilwa Alkaline Province, Malawi. *Journal of African Earth Sciences*, 20(3–4), 275–288. [https://doi.org/10.1016/0899-5362\(95\)00054-W](https://doi.org/10.1016/0899-5362(95)00054-W)
- Engelder, T. (1985). Loading paths to joint propagation during a tectonic cycle: An example from the Appalachian Plateau, U.S.A. *Journal of Structural Geology*, 7(3–4), 459–476. [https://doi.org/10.1016/0191-8141\(85\)90049-5](https://doi.org/10.1016/0191-8141(85)90049-5)
- Etheridge, M. A. (1986). On the reactivation of extensional fault systems. *Philosophical Transactions - Royal Society of London, Series A*, 317(1539), 179–194. <https://doi.org/10.1098/rsta.1986.0031>
- Fagereng, Å. (2013). Fault segmentation, deep rift earthquakes and crustal rheology: Insights from the 2009 Karonga sequence and seismicity in the Rukwa-Malawi rift zone. *Tectonophysics*, 601, 216–225. <https://doi.org/10.1016/j.tecto.2013.05.012>
- Flannery, J. W., & Rosendahl, B. R. (1990). The seismic stratigraphy of Lake Malawi, Africa: Implications for interpreting geological processes in lacustrine rifts. *Journal of African Earth Sciences*, 10(3), 519–548. [https://doi.org/10.1016/0899-5362\(90\)90104-M](https://doi.org/10.1016/0899-5362(90)90104-M)
- Fritz, H., Abdelsalam, M., Ali, K. A., Bingen, B., Collins, A. S., Fowler, A. R., et al. (2013). Orogen styles in the East African Orogen: A review of the Neoproterozoic to Cambrian tectonic evolution. *Journal of African Earth Sciences*, 86, 65–106. <https://doi.org/10.1016/j.jafrearsci.2013.06.004>
- Gaherty, J. B., Zheng, W., Shillington, D. J., Pritchard, M. E., Henderson, S. T., Chindandali, P. R. N., et al. (2019). Faulting processes during early-stage rifting: Seismic and geodetic analysis of the 2009–2010 Northern Malawi earthquake sequence. *Geophysical Journal International*, 217(3), 1767–1782. <https://doi.org/10.1093/gji/ggz119>
- Habgood, F. (1963). The geology of the country west of the Shire River between Chikwawa and Chiromo. Bulletin of the Geological Survey, Malawi, 14.
- Habgood, F., Holt, D. N., & Walshaw, R. D. (1973). The geology of the Thyolo Area. Bulletin of the Geological Survey, Malawi, 22.
- Hamiel, Y., Baer, G., Kalindekafu, L., Dombola, K., & Chindandali, P. (2012). Seismic and aseismic slip evolution and deformation associated with the 2009–2010 northern Malawi earthquake swarm, East African Rift. *Geophysical Journal International*, 191(3), 898–908. <https://doi.org/10.1111/j.1365-246X.2012.05673.x>
- Hampel, A., Li, T., & Maniatis, G. (2013). Contrasting strike-slip motions on thrust and normal faults: Implications for space-geodetic monitoring of surface deformation. *Geology*, 41(3), 299–302. <https://doi.org/10.1130/G33927.1>
- Hargrove, U. S., Hanson, R. E., Martin, M. W., Blenkinsop, T. G., Bowring, S. A., Walker, N., & Munyanyiwa, H. (2003). Tectonic evolution of the Zambezi orogenic belt: Geochronological, structural, and petrological constraints from northern Zimbabwe. *Precambrian Research*, 123(2–4), 159–186. [https://doi.org/10.1016/S0301-9268\(03\)00066-4](https://doi.org/10.1016/S0301-9268(03)00066-4)
- Healy, D., Blenkinsop, T. G., Timms, N. E., Meredith, P. G., Mitchell, T. M., & Cooke, M. L. (2015). Polymodal faulting: Time for a new angle on shear failure. *Journal of Structural Geology*, 80, 57–71. <https://doi.org/10.1016/j.jsg.2015.08.013>
- Hellebrekers, N., Niemeijer, A., Fagereng, Å., Manda, B., & Mvula, R. (2019). Lower crustal earthquakes in the East African Rift System: Insights from frictional properties of rock samples from the Malawi Rift. *EarthArXiv*. <https://doi.org/10.31223/osf.io/nu7rq>
- Henstra, G. A., Rotevatn, A., Gawthorpe, R. L., & Ravnås, R. (2015). Evolution of a major segmented normal fault during multiphase rifting: The origin of plan-view zigzag geometry. *Journal of Structural Geology*, 74, 45–63. <https://doi.org/10.1016/j.jsg.2015.02.005>
- Hodge, M., Biggs, J., Fagereng, A., Elliott, A., Mdala, H., & Mphepo, F. (2019). A semi-automated algorithm to quantify scarp morphology (SPARTA): Application to normal faults in southern Malawi. *Solid Earth*, 10(1), 27–57. <https://doi.org/10.5194/se-10-27-2019>
- Hodge, M., Biggs, J., Goda, K., & Aspinall, W. (2015). Assessing infrequent large earthquakes using geomorphology and geodesy: The Malawi Rift. *Natural Hazards*, 76(3), 1781–1806. <https://doi.org/10.1007/s11069-014-1572-y>
- Hodge, M., Fagereng, A., Biggs, J., & Mdala, H. (2018). Controls on early-rift geometry: New perspectives from the Bilila-Mtakataka Fault, Malawi. *Geophysical Research Letters*, 45, 3896–3905. <https://doi.org/10.1029/2018GL077343>
- Hollingsworth, A. D., Koehn, D., Dempster, T. J., & Aanyu, K. (2019). Structural controls on the interaction between basin fluids and a rift flank fault: Constraints from the Bwamba Fault, East African Rift. *Journal of Structural Geology*, 118, 236–249. <https://doi.org/10.1016/j.jsg.2018.10.012>
- Isaacs, A. J., Evans, J. P., Song, S.-R., & Kolesar, P. T. (2007). Structural, mineralogical, and geochemical characterization of the Chelungpu Thrust Fault, Taiwan. *Terrestrial, Atmospheric and Oceanic Sciences*, 18(2), 183. [https://doi.org/10.3319/TAO.2007.18.2.183\(TCDP\)](https://doi.org/10.3319/TAO.2007.18.2.183(TCDP))
- Jackson, J., & Blenkinsop, T. (1997). The Bilila-Mtakataka fault in Malawi: An active, 100-km long, normal fault segment in thick seismogenic crust. *Tectonics*, 16(1), 137–150. <https://doi.org/10.1029/96TC02494>
- Jaeger, J. C., Cook, N. G., & Zimmerman, R. (2007). *Fundamentals of rock mechanics* (4th ed.). Oxford: Wiley-Blackwell
- Johnson, S. P., De Waele, B., & Liyungu, K. A. (2006). U-Pb sensitive high-resolution ion microprobe (SHRIMP) zircon geochronology of granitoid rocks in eastern Zambia: Terrane subdivision of the Mesoproterozoic Southern Irumide Belt. *Tectonics*, 25, TC6004. <https://doi.org/10.1029/2006TC001977>
- Kamb, W. B. (1959). Ice petrofabric observations from Blue Glacier, Washington, in relation to theory and experiment. *Journal of Geophysical Research*, 64(11), 1891–1909. <https://doi.org/10.1029/JZ064i011p01891>
- Kolawole, F., Atekwana, E. A., Laó-Dávila, D. A., Abdelsalam, M. G., Chindandali, P. R., Salima, J., & Kalindekafu, L. (2018). Active deformation of Malawi Rift's North Basin hinge zone modulated by reactivation of preexisting Precambrian shear zone fabric. *Tectonics*, 37, 683–704. <https://doi.org/10.1002/2017TC004628>
- Kröner, A., Willner, A. P., Hegner, E., Jaekel, P., & Nemchin, A. (2001). Single zircon ages, PT evolution and Nd isotopic systematics of high-grade gneisses in southern Malawi and their bearing on the evolution of the Mozambique belt in southeastern Africa. *Precambrian Research*, 109(3–4), 257–291. [https://doi.org/10.1016/S0301-9268\(01\)00150-4](https://doi.org/10.1016/S0301-9268(01)00150-4)
- Laó-Dávila, D. A., Al-Salmi, H. S., Abdelsalam, M. G., & Atekwana, E. A. (2015). Hierarchical segmentation of the Malawi Rift: The influence of inherited lithospheric heterogeneity and kinematics in the evolution of continental rifts. *Tectonics*, 34, 2399–2417. <https://doi.org/10.1002/2015TC003953>
- Lavayssière, A., Drooff, C., Ebinger, C., Gallacher, R., Illsley-Kemp, F., Oliva, S. J., & Keir, D. (2019). Depth extent and kinematics of faulting in the Southern Tanganyika Rift, Africa. *Tectonics*, 38, 842–862. <https://doi.org/10.1029/2018TC005379>
- Leclère, H., & Fabbri, O. (2013). A new three-dimensional method of fault reactivation analysis. *Journal of Structural Geology*, 48, 153–161. <https://doi.org/10.1016/j.jsg.2012.11.004>
- Lisle, R. J., Orife, T. O., Arlegui, L., Liesa, C., & Srivastava, D. C. (2006). Favoured states of palaeostress in the Earth's crust: Evidence from fault-slip data. *Journal of Structural Geology*, 28(6), 1051–1066. <https://doi.org/10.1016/j.jsg.2006.03.012>
- Lisle, R. J., & Srivastava, D. C. (2004). Test of the frictional reactivation theory for faults and validity of fault-slip analysis. *Geology*, 32(7), 569. <https://doi.org/10.1130/G20408.1>

- Lockner, D. A. (1995). Rock failure. In *Rock Physics and Phase Relations: A Handbook of Physical Constants* (Vol. 3, pp. 127–147). Washington, DC: American Geophysical Union.
- Lopes Cardozo, G. G. O., & Behrmann, J. H. (2006). Kinematic analysis of the Upper Rhine Graben boundary fault system. *Journal of Structural Geology*, 28(6), 1028–1039. <https://doi.org/10.1016/j.jsg.2006.03.010>
- Manda, B. W. C., Cawood, P. A., Spencer, C. J., Prave, T., Robinson, R., & Roberts, N. M. W. (2019). Evolution of the Mozambique Belt in Malawi constrained by granitoid U-Pb, Sm-Nd and Lu-Hf isotopic data. *Gondwana Research*, 68, 93–107. <https://doi.org/10.1016/j.gr.2018.11.004>
- Manyozo, D. M., Mandla, A. T., & Phiri, F. R. (1972). The geology of the Lake Malombe area. Bulletin of the Geological Survey, Malawi, 33.
- Massironi, M., Bistacchi, A., & Menegon, L. (2011). Misoriented faults in exhumed metamorphic complexes: Rule or exception? *Earth and Planetary Science Letters*, 307(1–2), 233–239. <https://doi.org/10.1016/j.epsl.2011.04.041>
- McClay, K. R., & White, M. J. (1995). Analogue modelling of orthogonal and oblique rifting. *Marine and Petroleum Geology*, 12(2), 137–151. [https://doi.org/10.1016/0264-8172\(95\)92835-K](https://doi.org/10.1016/0264-8172(95)92835-K)
- Mesko, G. T., Class, C., Maqway, M. D., Boniface, N., Many, S., & Hemming, S. R. (2014). The timing of early magmatism and extension in the southern East African rift: Tracking geochemical source variability with <sup>40</sup>Ar/<sup>39</sup>Ar geochronology at the Rungwe Volcanic Province, SW Tanzania. In AGU Fall Meeting Abstracts.
- Moore, D. E., & Lockner, D. A. (2004). Crystallographic controls on the frictional behavior of dry and water-saturated sheet structure minerals. *Journal of Geophysical Research*, 109, B03401. <https://doi.org/10.1029/2003JB002582>
- Morley, C. K. (2010). Stress re-orientation along zones of weak fabrics in rifts: An explanation for pure extension in “oblique” rift segments? *Earth and Planetary Science Letters*, 297(3–4), 667–673. <https://doi.org/10.1016/j.epsl.2010.07.022>
- Morley, C. K., Haranya, C., Phoosongsee, W., Pongwapee, S., Kornasawan, A., & Wonganan, N. (2004). Activation of rift oblique and rift parallel pre-existing fabrics during extension and their effect on deformation style: Examples from the rifts of Thailand. *Journal of Structural Geology*, 26(10), 1803–1829. <https://doi.org/10.1016/j.jsg.2004.02.014>
- Morris, A., Ferrill, D. A., & Henderson, D. B. (1996). Slip-tendency analysis and fault reactivation. *Geology*, 24(3), 275. [https://doi.org/10.1130/0091-7613\(1996\)024<0275:STAAFR>2.3.CO;2](https://doi.org/10.1130/0091-7613(1996)024<0275:STAAFR>2.3.CO;2)
- Mortimer, E. J., Kirstein, L. A., Stuart, F. M., & Strecker, M. R. (2016). Spatio-temporal trends in normal-fault segmentation recorded by low-temperature thermochronology: Livingstone fault scarp, Malawi Rift, East African Rift System. *Earth and Planetary Science Letters*, 455, 62–72. <https://doi.org/10.1016/j.epsl.2016.08.040>
- Mortimer, E. J., Paton, D. A., Scholz, C. A., Strecker, M. R., & Blisniuk, P. (2007). Orthogonal to oblique rifting: Effect of rift basin orientation in the evolution of the North basin, Malawi Rift, East Africa. *Basin Research*, 19(3), 393–407. <https://doi.org/10.1111/j.1365-2117.2007.00332.x>
- Muluneh, A. A., Kidane, T., Corti, G., & Keir, D. (2018). Constraints on fault and crustal strength of the Main Ethiopian Rift from formal inversion of earthquake focal mechanism data. *Tectonophysics*, 731–732, 172–180. <https://doi.org/10.1016/j.tecto.2018.03.010>
- Mynatt, W. G., Beresh, S. C. M., Elifritz, E. A., Johnson, S., Mendez, K., Mayle, M., et al. (2017). Imaging of the subsurface expression of the Bilila-Mtakataka Fault using electrical resistivity in the Central Malawi Rift. In AGU Fall Meeting Abstracts.
- Norris, R. J., & Cooper, A. F. (1995). Origin of small-scale segmentation and transpressional thrusting along the Alpine Fault, New Zealand. *Geological Society of America Bulletin*, 107(2), 231–240. [https://doi.org/10.1130/0016-7606\(1995\)107<0231:OOSSSA>2.3.CO;2](https://doi.org/10.1130/0016-7606(1995)107<0231:OOSSSA>2.3.CO;2)
- Nyblade, A. A., & Langston, C. A. (1995). East African earthquakes below 20 km depth and their implications for crustal structure. *Geophysical Journal International*, 121(1), 49–62. <https://doi.org/10.1111/j.1365-246X.1995.tb03510.x>
- Petit, C., Déverchère, J., Houdry, F., Sankov, V. A., Melnikova, V. I., & Delvaux, D. (1996). Present-day stress field changes along the Baikal rift and tectonic implications. *Tectonics*, 15(6), 1171–1191. <https://doi.org/10.1029/96TC00624>
- Philippon, M., Willingshofer, E., Sokoutis, D., Corti, G., Sani, F., Bonini, M., & Cloetingh, S. (2015). Slip re-orientation in oblique rifts. *Geology*, 43(2), 147–150. <https://doi.org/10.1130/G36208.1>
- Pollard, D. D., Saltzer, S. D., & Rubin, A. M. (1993). Stress inversion methods: Are they based on faulty assumptions? *Journal of Structural Geology*, 15(8), 1045–1054. [https://doi.org/10.1016/0191-8141\(93\)90176-B](https://doi.org/10.1016/0191-8141(93)90176-B)
- Price, N. J. (1959). Mechanics of jointing in rocks. *Geological Magazine*, 96(2), 149–167. <https://doi.org/10.1017/S0016756800060040>
- Ring, U., Betzler, C., & Delvaux, D. (1992). Normal vs. strike-slip faulting during rift development in East Africa: The Malawi rift. *Geology*, 20(11), 1015–1018. [https://doi.org/10.1130/0091-7613\(1992\)020<1015:NVSSFD>2.3.CO;2](https://doi.org/10.1130/0091-7613(1992)020<1015:NVSSFD>2.3.CO;2)
- Roberts, E. M., Stevens, N. J., O'Connor, P. M., Dirks, P. H. G. M., Gottfried, M. D., Clyde, W. C., et al. (2012). Initiation of the western branch of the East African Rift coeval with the eastern branch. *Nature Geoscience*, 5(4), 289–294. <https://doi.org/10.1038/ngeo1432>
- Roberts, G. P. (1996). Variation in fault-slip directions along active and segmented normal fault systems. *Journal of Structural Geology*, 18(6), 835–845. [https://doi.org/10.1016/S0191-8141\(96\)80016-2](https://doi.org/10.1016/S0191-8141(96)80016-2)
- Sandwell, D., Mellors, R., Tong, X., Wei, M., & Wessel, P. (2011). Open radar interferometry software for mapping surface Deformation. *Eos, Transactions American Geophysical Union*, 92(28), 234. <https://doi.org/10.1029/2011EO280002>
- Saria, E., Calais, E., Stamps, D. S., Delvaux, D., & Hartnady, C. J. H. (2014). Present-day kinematics of the East African Rift. *Journal of Geophysical Research: Solid Earth*, 119, 3584–3600. <https://doi.org/10.1002/2013JB010901>
- Scott, D. L., Etheridge, M. A., & Rosendahl, B. R. (1992). Oblique-slip deformation in extensional terrains: A case study of the lakes Tanganyika and Malawi Rift Zones. *Tectonics*, 11(5), 998–1009. <https://doi.org/10.1029/92TC00821>
- Sibson, R. H. (1985). A note on fault reactivation. *Journal of Structural Geology*, 7(6), 751–754. [https://doi.org/10.1016/0191-8141\(85\)90150-6](https://doi.org/10.1016/0191-8141(85)90150-6)
- Sibson, R. H. (1998). Brittle failure mode plots for compressional and extensional tectonic regimes. *Journal of Structural Geology*, 20(5), 655–660. [https://doi.org/10.1016/S0191-8141\(98\)00116-3](https://doi.org/10.1016/S0191-8141(98)00116-3)
- Sibson, R. H., & Rowland, J. V. (2003). Stress, fluid pressure and structural permeability in seismogenic crust, North Island, New Zealand. *Geophysical Journal International*, 154(2), 584–594. <https://doi.org/10.1046/j.1365-246X.2003.01965.x>
- Smith, M., & Mosley, P. (1993). Crustal heterogeneity and basement influence on the development of the Kenya Rift, East Africa. *Tectonics*, 12(2), 591–606. <https://doi.org/10.1029/92TC01710>
- Stamps, D. S., Calais, E., Saria, E., Hartnady, C., Nocquet, J. M., Ebinger, C. J., & Fernandes, R. M. (2008). A kinematic model for the East African Rift. *Geophysical Research Letters*, 35, L05304. <https://doi.org/10.1029/2007GL032781>
- Stamps, D. S., Saria, E., & Kreemer, C. (2018). A geodetic strain rate model for the East African Rift System. *Scientific Reports*, 8(1), 732. <https://doi.org/10.1038/s41598-017-19097-w>
- Sutherland, R., Toy, V. G., Townend, J., Cox, S. C., Eccles, J. D., Faulkner, D. R., et al. (2012). Drilling reveals fluid control on architecture and rupture of the Alpine fault, New Zealand. *Geology*, 40(12), 1143–1146. <https://doi.org/10.1130/G33614.1>

- Tenthorey, E., & Cox, S. F. (2006). Cohesive strengthening of fault zones during the interseismic period: An experimental study. *Journal of Geophysical Research*, *111*, B09202. <https://doi.org/10.1029/2005JB004122>
- Twiss, R. J., & Unruh, J. R. (1998). Analysis of fault slip inversions: Do they constrain stress or strain rate? *Journal of Geophysical Research*, *103*(B6), 12,205–12,222. <https://doi.org/10.1029/98JB00612>
- U.S. Department of the Interior U.S. Geological Survey. (2018). M 5.5-24 km NE of Nsanje, Malawi (available at <https://earthquake.usgs.gov/earthquakes/eventpage/us1000d1cy#executive>, last accessed 26 Sept 2018).
- Versfelt, J., & Rosendahl, B. R. (1989). Relationships between pre-rift structure and rift architecture in Lakes Tanganyika and Malawi, East Africa. *Nature*, *337*(6205), 354–357. <https://doi.org/10.1038/337354a0>
- Villamor, P., Nicol, A., Seebeck, H., Rowland, J., Townsend, D., Massiot, C., et al. (2017). Tectonic structure and permeability in the Taupō Rift: new insights from analysis of LiDAR derived DEMs. In *Proceedings 39th New Zealand Geothermal Workshop* (Vol. 22, p. 24).
- Wallace, R. E. (1951). Geometry of shearing stress and relation to faulting. *The Journal of Geology*, *59*(2), 118–130. <https://doi.org/10.1086/625831>
- Walshaw, R. D. (1965). The geology of the Nchue-Balaka Area. Bulletin of the Geological Survey, Malawi, 19.
- Wedmore, L., Biggs, J., Williams, J. N., Fagereng, Å., Dulanya, Z., Mphepo, F., & Mdala, H. (2019). Distributed active fault scarps in southern Malawi and the implications for the evolution of strain in amagmatic continental rifts. EarthArXiv. <https://doi.org/10.31223/osf.io/tjchx>
- Wheeler, W. H., & Rosendahl, B. R. (1994). Geometry of the Livingstone Mountains Border Fault, Nyasa (Malawi) Rift, East Africa. *Tectonics*, *13*(2), 303–312. <https://doi.org/10.1029/93TC02314>
- Williams, J. N., Toy, V. G., Massiot, C., McNamara, D. D., Smith, S. A. F., & Mills, S. (2018). Controls on fault zone structure and brittle fracturing in the foliated hanging wall of the Alpine Fault. *Solid Earth*, *9*(2), 469–489. <https://doi.org/10.5194/se-9-469-2018>
- Withjack, M. O., & Jamison, W. R. (1986). Deformation produced by oblique rifting. *Tectonophysics*, *126*(2–4), 99–124. [https://doi.org/10.1016/0040-1951\(86\)90222-2](https://doi.org/10.1016/0040-1951(86)90222-2)